Ontario

We are committed to providing accessible customer service.
If you need accessible formats or communications supports, please contact us.

Nous tenons à améliorer l’accessibilité des services à la clientèle.
Si vous avez besoin de formats accessibles ou d’aide à la communication, veuillez nous contacter.

ASSESSMENT REPORT

March 21, 2023

Crystal Lake Project – Airborne Gravity Gradiometer and Magnetometer Survey

Pardee and Crooks Twp.
NTS#052A04

For:
Duffey Lake Holdings Inc.
666 Burrard Street, 25 Floor
Vancouver, BC
V6C 2X8

Prepared By:
Steven Flank, P.Geo, MSc.

Bayside Geoscience Inc.
1179 Carrick St. Unit C
Thunder Bay, ON
P7B 6M3

Contents

Assessment Report

CRYSTAL LAKE PROJECT – AIRBORNE GRAVITY GRADIOMETER AND MAGNETOMETER SURVEY

SUMMARY

Duffey Lake Holdings engaged Xcalibur Multiphysics to complete a high-sensitivity aeromagnetic and HeliFALCON™ Airborne Gravity Gradiometer (AGG) survey on the Crystal Lake Project, located 40km south of Thunder Bay, Ontario. Duffey Lake is completing the work under an earn-in agreement with Rio Tinto Exploration Canada (RTEC), who has owned the property since 2007.

The HeliFALCON™ is the only airborne gravity gradiometer system deployable in a helicopter and is optimized for airborne broadband geophysical explorations providing ultra-high-resolution data. It is done by using the Fourier method to transform the curvature gradients into gravity and the complete set of tensor components without the loss of resolution. This method significantly improves the accuracy of the longer wavelengths. The aeromagnetic data was collected at the same time. Five production flights were flown over the survey area. A total of 964 line-km's of data were acquired, of which 602.85 line km's were over RTEC mineral tenure.

The survey highlighted gravity and magnetic anomalies coincident with the interpreted extent of the Crystal Lake intrusion. This data will be implemented into Duffy Lake's proprietary stochastic inversion methods to further investigate the Crystal Lake Property for accumulations of Ni-Cu-PGE bearing sulfide mineralization.

INTRODUCTION

Between March 28th and April 2nd ,2022, Duffey Lake Holdings Inc. completed an Airborne Gravity Gradiometer and Magnetometer survey on the joint venture Crystal Lake Project which is 100% owned by Rio Tinto Exploration Canada Inc., located in the Thunder Bay Mining Division, Ontario, Canada. Duffey Lake Holdings contracted Xcalibur Multiphysics of Mississauga, ON to complete the program.

The Crystal Lake Project overlies the Great Lakes Nickel Deposit, which is hosted within the Crystal Lake Gabbro. A historic, non NI-43-101 compliant, resource of 40Mt @ 0.4% Cu and 0.2% Ni is reported in the Ontario Mineral Inventory description of the project.

Duffy Lake has engaged in exploration activities, including those reported here, to explore the project for economical concentrations of Ni-Cu-PGE bearing sulfides associated with the Crystal Lake Intrusion.

The coordinate system used throughout this report is in UTM NAD 83 Zone 16N.

1. LOCATION AND ACCESS

The Crystal Lake Property is located within the Thunder Bay Mining Division in Crooks and Pardee Township approximately 40 km south of the city of Thunder Bay (Figure 1).

The Crystal Lake Property is accessible by road indirectly from Highway 61 approximately 40 km south of Thunder Bay, continuing west for several kilometers along the Great Lakes Nickel gravel road. The Great Lakes Nickel Road is gated in 2 locations and crosses private property; therefore, permission of landowners is required to access the property (Figure 2). Various grown-in drill roads and trails are accessible from the Great Lake Nickel Road via UTV/ATV.

During the program, the contractors from Xcalibur Multiphysics worked between the period of March 28th and April 2nd ,2022. A daily commute was completed by truck from Thunder Bay to access the property, occasionally using an ATV/UTV to access areas with unfavorable road conditions.

2. PROPERTY OWNERSHIP AND CLAIMS

The Crystal Lake Property is in the Thunder Bay Mining Division and is comprised of 226 mining claims, 27 leased claims, and 34 mine land patents totaling 7,345 ha. All claims are 100% owned by Rio Tinto Exploration Canada Inc. with operations being carried out by Duffey Lake Holding Inc. Claim locations are shown in Figure 2.

Figure 1: Crystal Lake Property Location.

3. EXPLORATION HISTORY

Extensive mineral exploration has occurred in the Crystal Lake area since the discovery of copper-nickel mineralized float in the area in 1936. A summary of exploration is presented below in Table 1.

Table 1: Exploration history of the Crystal Lake Project

Company	**Year**	**Activity**	**Target Area**
United States Smelting, Refining and Mining Co.	1936	Conducted exploration looking for the source of copper-nickel mineralized float boulders.	Crystal Lake Area
Mattawin Gold Mines Ltd.	1952	Staked property and optioned to Falconbridge Nickel Mines	Crystal Lake Area
Falconbridge Nickel Mines	1952-1953	Surface work including trenching	Crystal Lake Area
Mattawin Gold Mines Ltd.	1954	6 DDH totaling 3471 ft	Crystal Lake Area
Mogul Mining Corp. Ltd.	1957	Optioned property and drilled 7 DDH totaling 5556 ft and undertook mill testing	Crystal Lake Area
Great Lakes Nickel Corp. Ltd.	1964-1970	Acquired option for property and conducted surface exploration including 47803m of drilling and started 37m adit. 19 underground DDH were completed totaling 392 m.	Crystal Lake Area

Great Lakes Nickel Corp. Ltd.	1972	Drove 522 m development portal and drift. Conducted over 12000 m of surface and underground diamond drilling. Plant-site surveys, bulk sampling, metallurgical and feasibility tests were conducted, largely financed by a Swedish company, Boliden Aktiebolag. A reserve was defined on the tip of the northern CLG arm containing proven and indicated reserves of 41.4 MT grading 0.334% Cu, 0.183% Ni, 0.69 g/t Pd. 0.21 g/t Pt, 0.01 g/t Rh, 0.04 g/t Au, and 2.06 g/t Ag.	Crystal Lake Area
Great Lakes Nickel Corp. Ltd.	1974	Mine development suspended in October due to escalating costs, high interest rates and uncertain metal prices.	Crystal Lake Area
Fleck Resources Ltd.	1986-87	Completed geological mapping and sampling, relogged and assayed more than 9144 m of historic drill core and drilled 6 DDH.	Crystal Lake Area

Great Lakes Nickel Corp. Ltd.	2000	Sampling of historical drill core and block modelling to develop a resource estimate.	Crystal Lake Area
Kennecott Canada Exploration Inc.	2007	Staked, airborne electromagnetic survey, airborne magnetic survey.	Crystal Lake Area
Rio Tinto Exploration Canada Inc.	2011	Optioned the property from Great Lakes Nickel in November	Crystal Lake Area
Rio Tinto Exploration Canada Inc.	2013-2014	Re-assayed historic drill holes drilled 5 DDH totaling 3170.03 m and conducted downhole geophysics.	Crystal Lake Area
Rio Tinto Exploration Canada Inc.	2015	Completed 2 of 3 reported holes along the Great Lakes Nickel plunge trend.	Crystal Lake Area
Sean O'Brien	2018	Lakehead University Master's thesis on the petrology of the Crystal Lake Gabbro and the Mount Mollie Dyke, Midcontinent Rift, Northwest Ontario	Crystal Lake and Mount Mollie Area

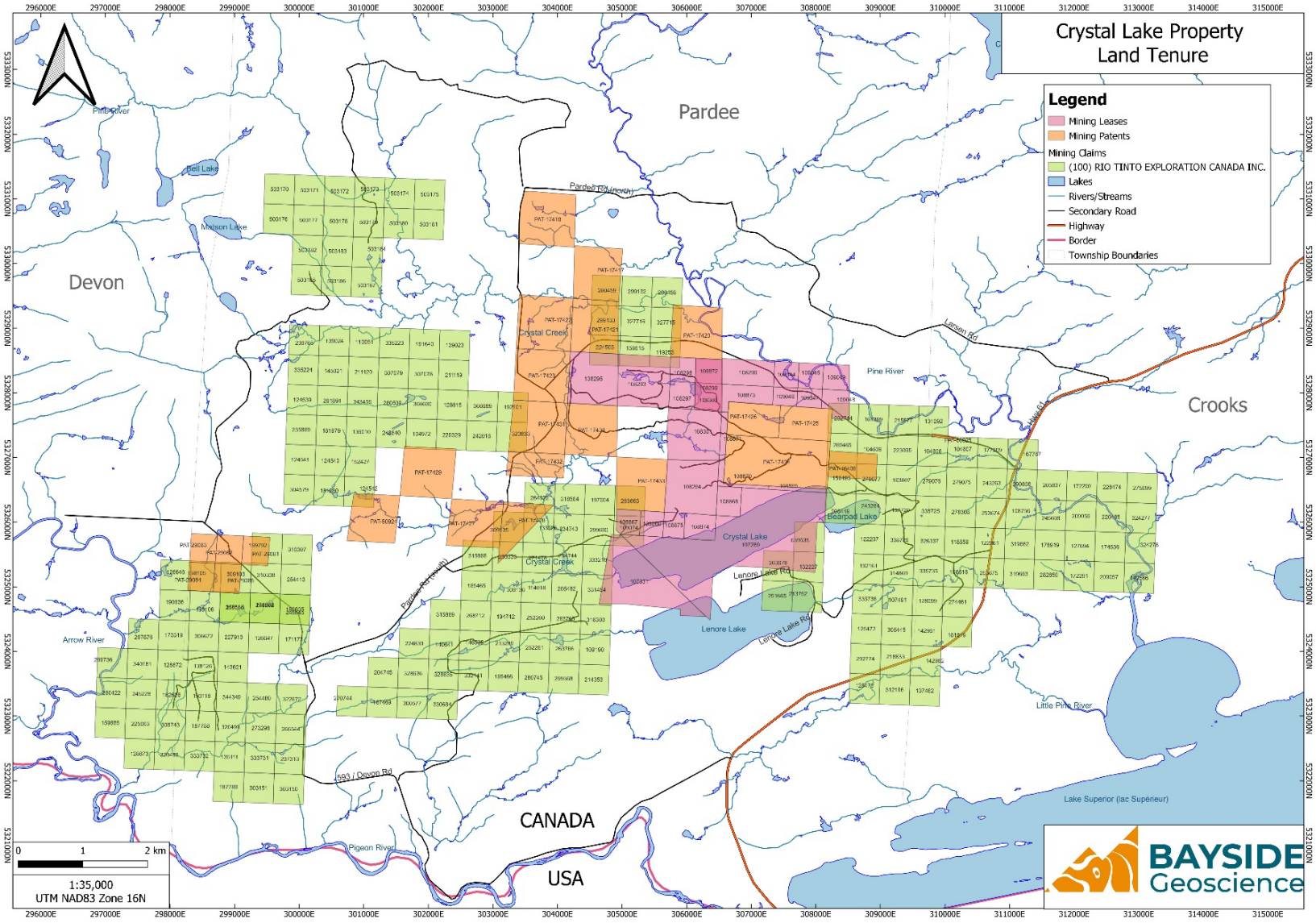

Figure 2:Crystal Lake Property Claim Map

OPERATIONAL CLAIM DETAILS

MINING CLAIMS

TENURE_NUM	AREA_HECTARES	TITLE_TY_1	ISSUE_DATE	CLAIM_DUE_	HOLDER
639535	21.59	Single Cell Mining Claim	2/25/2021	2/25/2023	(100) RIO TINTO EXPLORATION CANADA INC.
104607	21.58	Single Cell Mining Claim	4/10/2018	3/6/2023	(100) RIO TINTO EXPLORATION CANADA INC.
104608	21.58	Single Cell Mining Claim	4/10/2018	3/6/2023	(100) RIO TINTO EXPLORATION CANADA INC.
104609	21.58	Single Cell Mining Claim	4/10/2018	3/6/2023	(100) RIO TINTO EXPLORATION CANADA INC.
108756	21.58	Single Cell Mining Claim	4/10/2018	3/6/2023	(100) RIO TINTO EXPLORATION CANADA INC.
118559	21.59	Single Cell Mining Claim	4/10/2018	3/6/2023	(100) RIO TINTO EXPLORATION CANADA INC.
122961	21.59	Single Cell Mining Claim	4/10/2018	3/6/2023	(100) RIO TINTO EXPLORATION CANADA INC.
125472	21.59	Boundary Cell Mining Claim	4/10/2018	3/6/2023	(100) RIO TINTO EXPLORATION CANADA INC.
125473	21.59	Boundary Cell Mining Claim	4/10/2018	3/6/2023	(100) RIO TINTO EXPLORATION CANADA INC.
128099	21.59	Single Cell Mining Claim	4/10/2018	3/6/2023	(100) RIO TINTO EXPLORATION CANADA INC.
127694	21.59	Single Cell Mining Claim	4/10/2018	3/6/2023	(100) RIO TINTO EXPLORATION CANADA INC.
131292	21.58	Single Cell Mining Claim	4/10/2018	3/6/2023	(100) RIO TINTO EXPLORATION CANADA INC.
137462	21.59	Single Cell Mining Claim	4/10/2018	3/6/2023	(100) RIO TINTO EXPLORATION CANADA INC.
142961	21.59	Single Cell Mining Claim	4/10/2018	3/6/2023	(100) RIO TINTO EXPLORATION CANADA INC.
142962	21.59	Single Cell Mining Claim	4/10/2018	3/6/2023	(100) RIO TINTO EXPLORATION CANADA INC.
156493	21.58	Single Cell Mining Claim	4/10/2018	3/6/2023	(100) RIO TINTO EXPLORATION CANADA INC.
157720	21.58	Single Cell Mining Claim	4/10/2018	3/6/2023	(100) RIO TINTO EXPLORATION CANADA INC.
163807	21.58	Single Cell Mining Claim	4/10/2018	3/6/2023	(100) RIO TINTO EXPLORATION CANADA INC.
161399	21.58	Single Cell Mining Claim	4/10/2018	3/6/2023	(100) RIO TINTO EXPLORATION CANADA INC.
167767	21.58	Single Cell Mining Claim	4/10/2018	3/6/2023	(100) RIO TINTO EXPLORATION CANADA INC.
172290	21.58	Single Cell Mining Claim	4/10/2018	3/6/2023	(100) RIO TINTO EXPLORATION CANADA INC.
172291	21.59	Single Cell Mining Claim	4/10/2018	3/6/2023	(100) RIO TINTO EXPLORATION CANADA INC.
174536	21.59	Single Cell Mining Claim	4/10/2018	3/6/2023	(100) RIO TINTO EXPLORATION CANADA INC.
177209	21.58	Single Cell Mining Claim	4/10/2018	3/6/2023	(100) RIO TINTO EXPLORATION CANADA INC.
178919	21.59	Single Cell Mining Claim	4/10/2018	3/6/2023	(100) RIO TINTO EXPLORATION CANADA INC.
181619	21.59	Single Cell Mining Claim	4/10/2018	3/6/2023	(100) RIO TINTO EXPLORATION CANADA INC.
190566	21.59	Single Cell Mining Claim	4/10/2018	3/6/2023	(100) RIO TINTO EXPLORATION CANADA INC.
198516	21.59	Single Cell Mining Claim	4/10/2018	3/6/2023	(100) RIO TINTO EXPLORATION CANADA INC.
205837	21.58	Single Cell Mining Claim	4/10/2018	3/6/2023	(100) RIO TINTO EXPLORATION CANADA INC.
208449	21.58	Single Cell Mining Claim	4/10/2018	3/6/2023	(100) RIO TINTO EXPLORATION CANADA INC.
209056	21.58	Single Cell Mining Claim	4/10/2018	3/6/2023	(100) RIO TINTO EXPLORATION CANADA INC.
209057	21.59	Single Cell Mining Claim	4/10/2018	3/6/2023	(100) RIO TINTO EXPLORATION CANADA INC.
215577	21.58	Single Cell Mining Claim	4/10/2018	3/6/2023	(100) RIO TINTO EXPLORATION CANADA INC.
218833	21.59	Single Cell Mining Claim	4/10/2018	3/6/2023	(100) RIO TINTO EXPLORATION CANADA INC.
220485	21.58	Single Cell Mining Claim	4/10/2018	3/6/2023	(100) RIO TINTO EXPLORATION CANADA INC.
223095	21.58	Single Cell Mining Claim	4/10/2018	3/6/2023	(100) RIO TINTO EXPLORATION CANADA INC.
228474	21.58	Single Cell Mining Claim	4/10/2018	3/6/2023	(100) RIO TINTO EXPLORATION CANADA INC.
232744	21.58	Single Cell Mining Claim	4/10/2018	3/6/2023	(100) RIO TINTO EXPLORATION CANADA INC.
243263	21.58	Single Cell Mining Claim	4/10/2018	3/6/2023	(100) RIO TINTO EXPLORATION CANADA INC.
243264	21.58	Single Cell Mining Claim	4/10/2018	3/6/2023	(100) RIO TINTO EXPLORATION CANADA INC.
245608	21.58	Single Cell Mining Claim	4/10/2018	3/6/2023	(100) RIO TINTO EXPLORATION CANADA INC.
253674	21.58	Single Cell Mining Claim	4/10/2018	3/6/2023	(100) RIO TINTO EXPLORATION CANADA INC.
253675	21.59	Single Cell Mining Claim	4/10/2018	3/6/2023	(100) RIO TINTO EXPLORATION CANADA INC.
269465	21.58	Single Cell Mining Claim	4/10/2018	3/6/2023	(100) RIO TINTO EXPLORATION CANADA INC.
274461	21.59	Single Cell Mining Claim	4/10/2018	3/6/2023	(100) RIO TINTO EXPLORATION CANADA INC.
275699	21.58	Single Cell Mining Claim	4/10/2018	3/6/2023	(100) RIO TINTO EXPLORATION CANADA INC.
278308	21.58	Single Cell Mining Claim	4/10/2018	3/6/2023	(100) RIO TINTO EXPLORATION CANADA INC.
279075	21.58	Single Cell Mining Claim	4/10/2018	3/6/2023	(100) RIO TINTO EXPLORATION CANADA INC.
279076	21.58	Single Cell Mining Claim	4/10/2018	3/6/2023	(100) RIO TINTO EXPLORATION CANADA INC.
279077	21.58	Single Cell Mining Claim	4/10/2018	3/6/2023	(100) RIO TINTO EXPLORATION CANADA INC.
282850	21.59	Single Cell Mining Claim	4/10/2018	3/6/2023	(100) RIO TINTO EXPLORATION CANADA INC.
290608	21.58	Single Cell Mining Claim	4/10/2018	3/6/2023	(100) RIO TINTO EXPLORATION CANADA INC.
292774	21.59	Boundary Cell Mining Claim	4/10/2018	3/6/2023	(100) RIO TINTO EXPLORATION CANADA INC.
305445	21.59	Single Cell Mining Claim	4/10/2018	3/6/2023	(100) RIO TINTO EXPLORATION CANADA INC.
312196	21.59	Single Cell Mining Claim	4/10/2018	3/6/2023	(100) RIO TINTO EXPLORATION CANADA INC.
319662	21.59	Single Cell Mining Claim	4/10/2018	3/6/2023	(100) RIO TINTO EXPLORATION CANADA INC.
319663	21.59	Single Cell Mining Claim	4/10/2018	3/6/2023	(100) RIO TINTO EXPLORATION CANADA INC.
324277	21.58	Single Cell Mining Claim	4/10/2018	3/6/2023	(100) RIO TINTO EXPLORATION CANADA INC.
324278	21.59	Single Cell Mining Claim	4/10/2018	3/6/2023	(100) RIO TINTO EXPLORATION CANADA INC.
326337	21.59	Boundary Cell Mining Claim	4/10/2018	3/6/2023	(100) RIO TINTO EXPLORATION CANADA INC.
335735	21.59	Boundary Cell Mining Claim	4/10/2018	3/6/2023	(100) RIO TINTO EXPLORATION CANADA INC.
338725	21.58	Single Cell Mining Claim	4/10/2018	3/6/2023	(100) RIO TINTO EXPLORATION CANADA INC.
338726	21.59	Boundary Cell Mining Claim	4/10/2018	3/6/2023	(100) RIO TINTO EXPLORATION CANADA INC.
109190	21.59	Single Cell Mining Claim	4/10/2018	3/28/2023	(100) RIO TINTO EXPLORATION CANADA INC.
109074	21.59	Single Cell Mining Claim	4/10/2018	3/28/2023	(100) RIO TINTO EXPLORATION CANADA INC.
114018	21.59	Single Cell Mining Claim	4/10/2018	3/28/2023	(100) RIO TINTO EXPLORATION CANADA INC.
133926	21.59	Single Cell Mining Claim	4/10/2018	3/28/2023	(100) RIO TINTO EXPLORATION CANADA INC.
140641	21.59	Single Cell Mining Claim	4/10/2018	3/28/2023	(100) RIO TINTO EXPLORATION CANADA INC.
146595	21.59	Single Cell Mining Claim	4/10/2018	3/28/2023	(100) RIO TINTO EXPLORATION CANADA INC.
165465	21.59	Single Cell Mining Claim	4/10/2018	3/28/2023	(100) RIO TINTO EXPLORATION CANADA INC.
165466	21.59	Single Cell Mining Claim	4/10/2018	3/28/2023	(100) RIO TINTO EXPLORATION CANADA INC.
167469	21.6	Single Cell Mining Claim	4/10/2018	3/28/2023	(100) RIO TINTO EXPLORATION CANADA INC.
194742	21.59	Single Cell Mining Claim	4/10/2018	3/28/2023	(100) RIO TINTO EXPLORATION CANADA INC.
197004	21.58	Single Cell Mining Claim	4/10/2018	3/28/2023	(100) RIO TINTO EXPLORATION CANADA INC.

TENURE_NUM	AREA_HECTARES	TITLE_TY_1	ISSUE_DATE	CLAIM_DUE_	HOLDER
204745	21.59	Single Cell Mining Claim	4/10/2018	3/28/2023	(100) RIO TINTO EXPLORATION CANADA INC.
205482	21.59	Single Cell Mining Claim	4/10/2018	3/28/2023	(100) RIO TINTO EXPLORATION CANADA INC.
213289	21.59	Single Cell Mining Claim	4/10/2018	3/28/2023	(100) RIO TINTO EXPLORATION CANADA INC.
214353	21.59	Single Cell Mining Claim	4/10/2018	3/28/2023	(100) RIO TINTO EXPLORATION CANADA INC.
224839	21.59	Single Cell Mining Claim	4/10/2018	3/28/2023	(100) RIO TINTO EXPLORATION CANADA INC.
234743	21.59	Single Cell Mining Claim	4/10/2018	3/28/2023	(100) RIO TINTO EXPLORATION CANADA INC.
234744	21.59	Single Cell Mining Claim	4/10/2018	3/28/2023	(100) RIO TINTO EXPLORATION CANADA INC.
250033	21.59	Single Cell Mining Claim	4/10/2018	3/28/2023	(100) RIO TINTO EXPLORATION CANADA INC.
252260	21.59	Single Cell Mining Claim	4/10/2018	3/28/2023	(100) RIO TINTO EXPLORATION CANADA INC.
252261	21.59	Single Cell Mining Claim	4/10/2018	3/28/2023	(100) RIO TINTO EXPLORATION CANADA INC.
264022	21.58	Single Cell Mining Claim	4/10/2018	3/28/2023	(100) RIO TINTO EXPLORATION CANADA INC.
263765	21.59	Single Cell Mining Claim	4/10/2018	3/28/2023	(100) RIO TINTO EXPLORATION CANADA INC.
263766	21.59	Single Cell Mining Claim	4/10/2018	3/28/2023	(100) RIO TINTO EXPLORATION CANADA INC.
268712	21.59	Single Cell Mining Claim	4/10/2018	3/28/2023	(100) RIO TINTO EXPLORATION CANADA INC.
271478	21.59	Single Cell Mining Claim	4/10/2018	3/28/2023	(100) RIO TINTO EXPLORATION CANADA INC.
270744	21.6	Single Cell Mining Claim	4/10/2018	3/28/2023	(100) RIO TINTO EXPLORATION CANADA INC.
280745	21.59	Single Cell Mining Claim	4/10/2018	3/28/2023	(100) RIO TINTO EXPLORATION CANADA INC.
299690	21.59	Single Cell Mining Claim	4/10/2018	3/28/2023	(100) RIO TINTO EXPLORATION CANADA INC.
299368	21.59	Single Cell Mining Claim	4/10/2018	3/28/2023	(100) RIO TINTO EXPLORATION CANADA INC.
300577	21.6	Single Cell Mining Claim	4/10/2018	3/28/2023	(100) RIO TINTO EXPLORATION CANADA INC.
309135	21.59	Single Cell Mining Claim	4/10/2018	3/28/2023	(100) RIO TINTO EXPLORATION CANADA INC.
309136	21.59	Single Cell Mining Claim	4/10/2018	3/28/2023	(100) RIO TINTO EXPLORATION CANADA INC.
315868	21.59	Single Cell Mining Claim	4/10/2018	3/28/2023	(100) RIO TINTO EXPLORATION CANADA INC.
315869	21.59	Single Cell Mining Claim	4/10/2018	3/28/2023	(100) RIO TINTO EXPLORATION CANADA INC.
318300	21.59	Single Cell Mining Claim	4/10/2018	3/28/2023	(100) RIO TINTO EXPLORATION CANADA INC.
318564	21.58	Single Cell Mining Claim	4/10/2018	3/28/2023	(100) RIO TINTO EXPLORATION CANADA INC.
328635	21.59	Single Cell Mining Claim	4/10/2018	3/28/2023	(100) RIO TINTO EXPLORATION CANADA INC.
328636	21.59	Single Cell Mining Claim	4/10/2018	3/28/2023	(100) RIO TINTO EXPLORATION CANADA INC.
331454	21.59	Single Cell Mining Claim	4/10/2018	3/28/2023	(100) RIO TINTO EXPLORATION CANADA INC.
332141	21.59	Single Cell Mining Claim	4/10/2018	3/28/2023	(100) RIO TINTO EXPLORATION CANADA INC.
333210	21.59	Single Cell Mining Claim	4/10/2018	3/28/2023	(100) RIO TINTO EXPLORATION CANADA INC.
330684	21.6	Single Cell Mining Claim	4/10/2018	3/28/2023	(100) RIO TINTO EXPLORATION CANADA INC.
503170	21.57	Single Cell Mining Claim	4/10/2018	4/10/2023	(100) RIO TINTO EXPLORATION CANADA INC.
503171	21.57	Single Cell Mining Claim	4/10/2018	4/10/2023	(100) RIO TINTO EXPLORATION CANADA INC.
503172	21.57	Single Cell Mining Claim	4/10/2018	4/10/2023	(100) RIO TINTO EXPLORATION CANADA INC.
503173	21.57	Single Cell Mining Claim	4/10/2018	4/10/2023	(100) RIO TINTO EXPLORATION CANADA INC.
503174	21.57	Single Cell Mining Claim	4/10/2018	4/10/2023	(100) RIO TINTO EXPLORATION CANADA INC.
503175	21.57	Single Cell Mining Claim	4/10/2018	4/10/2023	(100) RIO TINTO EXPLORATION CANADA INC.
503176	21.57	Single Cell Mining Claim	4/10/2018	4/10/2023	(100) RIO TINTO EXPLORATION CANADA INC.
503177	21.57	Single Cell Mining Claim	4/10/2018	4/10/2023	(100) RIO TINTO EXPLORATION CANADA INC.
503178	21.57	Single Cell Mining Claim	4/10/2018	4/10/2023	(100) RIO TINTO EXPLORATION CANADA INC.
503179	21.57	Single Cell Mining Claim	4/10/2018	4/10/2023	(100) RIO TINTO EXPLORATION CANADA INC.
503180	21.57	Single Cell Mining Claim	4/10/2018	4/10/2023	(100) RIO TINTO EXPLORATION CANADA INC.
503181	21.57	Single Cell Mining Claim	4/10/2018	4/10/2023	(100) RIO TINTO EXPLORATION CANADA INC.
503182	21.57	Single Cell Mining Claim	4/10/2018	4/10/2023	(100) RIO TINTO EXPLORATION CANADA INC.
503183	21.57	Single Cell Mining Claim	4/10/2018	4/10/2023	(100) RIO TINTO EXPLORATION CANADA INC.
503184	21.57	Single Cell Mining Claim	4/10/2018	4/10/2023	(100) RIO TINTO EXPLORATION CANADA INC.
503185	21.57	Single Cell Mining Claim	4/10/2018	4/10/2023	(100) RIO TINTO EXPLORATION CANADA INC.
503186	21.57	Single Cell Mining Claim	4/10/2018	4/10/2023	(100) RIO TINTO EXPLORATION CANADA INC.
503187	21.57	Single Cell Mining Claim	4/10/2018	4/10/2023	(100) RIO TINTO EXPLORATION CANADA INC.
176272	21.59	Boundary Cell Mining Claim	4/10/2018	6/4/2023	(100) RIO TINTO EXPLORATION CANADA INC.
199792	21.59	Single Cell Mining Claim	4/10/2018	6/4/2023	(100) RIO TINTO EXPLORATION CANADA INC.
249845	21.59	Boundary Cell Mining Claim	4/10/2018	6/4/2023	(100) RIO TINTO EXPLORATION CANADA INC.
254413	21.59	Single Cell Mining Claim	4/10/2018	6/4/2023	(100) RIO TINTO EXPLORATION CANADA INC.
268588	21.59	Boundary Cell Mining Claim	4/10/2018	6/4/2023	(100) RIO TINTO EXPLORATION CANADA INC.
309103	21.59	Single Cell Mining Claim	4/10/2018	6/4/2023	(100) RIO TINTO EXPLORATION CANADA INC.
310307	21.59	Single Cell Mining Claim	4/10/2018	6/4/2023	(100) RIO TINTO EXPLORATION CANADA INC.
310308	21.59	Single Cell Mining Claim	4/10/2018	6/4/2023	(100) RIO TINTO EXPLORATION CANADA INC.
107491	21.59	Single Cell Mining Claim	4/10/2018	6/24/2023	(100) RIO TINTO EXPLORATION CANADA INC.
192161	21.59	Boundary Cell Mining Claim	4/10/2018	6/24/2023	(100) RIO TINTO EXPLORATION CANADA INC.
314869	21.59	Boundary Cell Mining Claim	4/10/2018	6/24/2023	(100) RIO TINTO EXPLORATION CANADA INC.
335736	21.59	Single Cell Mining Claim	4/10/2018	6/24/2023	(100) RIO TINTO EXPLORATION CANADA INC.
122207	21.59	Boundary Cell Mining Claim	4/10/2018	7/14/2023	(100) RIO TINTO EXPLORATION CANADA INC.
104972	21.58	Single Cell Mining Claim	4/10/2018	9/18/2023	(100) RIO TINTO EXPLORATION CANADA INC.
110051	21.57	Single Cell Mining Claim	4/10/2018	9/18/2023	(100) RIO TINTO EXPLORATION CANADA INC.
119253	21.57	Single Cell Mining Claim	4/10/2018	9/18/2023	(100) RIO TINTO EXPLORATION CANADA INC.
124539	21.58	Single Cell Mining Claim	4/10/2018	9/18/2023	(100) RIO TINTO EXPLORATION CANADA INC.
124540	21.58	Single Cell Mining Claim	4/10/2018	9/18/2023	(100) RIO TINTO EXPLORATION CANADA INC.
124541	21.58	Single Cell Mining Claim	4/10/2018	9/18/2023	(100) RIO TINTO EXPLORATION CANADA INC.
124542	21.58	Single Cell Mining Claim	4/10/2018	9/18/2023	(100) RIO TINTO EXPLORATION CANADA INC.
128615	21.58	Single Cell Mining Claim	4/10/2018	9/18/2023	(100) RIO TINTO EXPLORATION CANADA INC.
136010	21.58	Single Cell Mining Claim	4/10/2018	9/18/2023	(100) RIO TINTO EXPLORATION CANADA INC.
139023	21.57	Single Cell Mining Claim	4/10/2018	9/18/2023	(100) RIO TINTO EXPLORATION CANADA INC.
139024	21.57	Single Cell Mining Claim	4/10/2018	9/18/2023	(100) RIO TINTO EXPLORATION CANADA INC.
145021	21.58	Single Cell Mining Claim	4/10/2018	9/18/2023	(100) RIO TINTO EXPLORATION CANADA INC.

TENURE_NUM	AREA_HECTARES	TITLE_TY_1	ISSUE_DATE	CLAIM_DUE_	HOLDER
152427	21.58	Single Cell Mining Claim	4/10/2018	9/18/2023	(100) RIO TINTO EXPLORATION CANADA INC.
159615	21.57	Single Cell Mining Claim	4/10/2018	9/18/2023	(100) RIO TINTO EXPLORATION CANADA INC.
181979	21.58	Single Cell Mining Claim	4/10/2018	9/18/2023	(100) RIO TINTO EXPLORATION CANADA INC.
181980	21.58	Single Cell Mining Claim	4/10/2018	9/18/2023	(100) RIO TINTO EXPLORATION CANADA INC.
191640	21.57	Single Cell Mining Claim	4/10/2018	9/18/2023	(100) RIO TINTO EXPLORATION CANADA INC.
192101	21.58	Single Cell Mining Claim	4/10/2018	9/18/2023	(100) RIO TINTO EXPLORATION CANADA INC.
211119	21.58	Single Cell Mining Claim	4/10/2018	9/18/2023	(100) RIO TINTO EXPLORATION CANADA INC.
211120	21.58	Single Cell Mining Claim	4/10/2018	9/18/2023	(100) RIO TINTO EXPLORATION CANADA INC.
224503	21.57	Single Cell Mining Claim	4/10/2018	9/18/2023	(100) RIO TINTO EXPLORATION CANADA INC.
229329	21.58	Single Cell Mining Claim	4/10/2018	9/18/2023	(100) RIO TINTO EXPLORATION CANADA INC.
235869	21.58	Single Cell Mining Claim	4/10/2018	9/18/2023	(100) RIO TINTO EXPLORATION CANADA INC.
239765	21.57	Single Cell Mining Claim	4/10/2018	9/18/2023	(100) RIO TINTO EXPLORATION CANADA INC.
242016	21.58	Single Cell Mining Claim	4/10/2018	9/18/2023	(100) RIO TINTO EXPLORATION CANADA INC.
248840	21.58	Single Cell Mining Claim	4/10/2018	9/18/2023	(100) RIO TINTO EXPLORATION CANADA INC.
260509	21.58	Single Cell Mining Claim	4/10/2018	9/18/2023	(100) RIO TINTO EXPLORATION CANADA INC.
280458	21.57	Single Cell Mining Claim	4/10/2018	9/18/2023	(100) RIO TINTO EXPLORATION CANADA INC.
280459	21.57	Single Cell Mining Claim	4/10/2018	9/18/2023	(100) RIO TINTO EXPLORATION CANADA INC.
291891	21.58	Single Cell Mining Claim	4/10/2018	9/18/2023	(100) RIO TINTO EXPLORATION CANADA INC.
299132	21.57	Single Cell Mining Claim	4/10/2018	9/18/2023	(100) RIO TINTO EXPLORATION CANADA INC.
299133	21.57	Single Cell Mining Claim	4/10/2018	9/18/2023	(100) RIO TINTO EXPLORATION CANADA INC.
304579	21.58	Single Cell Mining Claim	4/10/2018	9/18/2023	(100) RIO TINTO EXPLORATION CANADA INC.
307079	21.58	Single Cell Mining Claim	4/10/2018	9/18/2023	(100) RIO TINTO EXPLORATION CANADA INC.
307078	21.58	Single Cell Mining Claim	4/10/2018	9/18/2023	(100) RIO TINTO EXPLORATION CANADA INC.
308689	21.58	Single Cell Mining Claim	4/10/2018	9/18/2023	(100) RIO TINTO EXPLORATION CANADA INC.
308690	21.58	Single Cell Mining Claim	4/10/2018	9/18/2023	(100) RIO TINTO EXPLORATION CANADA INC.
323833	21.58	Single Cell Mining Claim	4/10/2018	9/18/2023	(100) RIO TINTO EXPLORATION CANADA INC.
327715	21.57	Single Cell Mining Claim	4/10/2018	9/18/2023	(100) RIO TINTO EXPLORATION CANADA INC.
327716	21.57	Single Cell Mining Claim	4/10/2018	9/18/2023	(100) RIO TINTO EXPLORATION CANADA INC.
335223	21.57	Single Cell Mining Claim	4/10/2018	9/18/2023	(100) RIO TINTO EXPLORATION CANADA INC.
335224	21.58	Single Cell Mining Claim	4/10/2018	9/18/2023	(100) RIO TINTO EXPLORATION CANADA INC.
343456	21.58	Single Cell Mining Claim	4/10/2018	9/18/2023	(100) RIO TINTO EXPLORATION CANADA INC.
126646	21.59	Single Cell Mining Claim	4/10/2018	3/21/2024	(100) RIO TINTO EXPLORATION CANADA INC.
132227	21.59	Single Cell Mining Claim	4/10/2018	9/18/2024	(100) RIO TINTO EXPLORATION CANADA INC.
213752	21.59	Single Cell Mining Claim	4/10/2018	9/18/2024	(100) RIO TINTO EXPLORATION CANADA INC.
251665	21.59	Single Cell Mining Claim	4/10/2018	9/18/2024	(100) RIO TINTO EXPLORATION CANADA INC.
263663	21.58	Single Cell Mining Claim	4/10/2018	9/18/2024	(100) RIO TINTO EXPLORATION CANADA INC.
263678	21.59	Single Cell Mining Claim	4/10/2018	9/18/2024	(100) RIO TINTO EXPLORATION CANADA INC.
344349	21.6	Single Cell Mining Claim	4/10/2018	3/21/2025	(100) RIO TINTO EXPLORATION CANADA INC.
126647	21.59	Single Cell Mining Claim	4/10/2018	3/21/2025	(100) RIO TINTO EXPLORATION CANADA INC.
135111	21.6	Single Cell Mining Claim	4/10/2018	3/21/2025	(100) RIO TINTO EXPLORATION CANADA INC.
138105	21.59	Single Cell Mining Claim	4/10/2018	3/21/2025	(100) RIO TINTO EXPLORATION CANADA INC.
138106	21.59	Single Cell Mining Claim	4/10/2018	3/21/2025	(100) RIO TINTO EXPLORATION CANADA INC.
138126	21.59	Single Cell Mining Claim	4/10/2018	3/21/2025	(100) RIO TINTO EXPLORATION CANADA INC.
143621	21.59	Single Cell Mining Claim	4/10/2018	3/21/2025	(100) RIO TINTO EXPLORATION CANADA INC.
155185	21.59	Boundary Cell Mining Claim	4/10/2018	3/21/2025	(100) RIO TINTO EXPLORATION CANADA INC.
173319	21.59	Single Cell Mining Claim	4/10/2018	3/21/2025	(100) RIO TINTO EXPLORATION CANADA INC.
171173	21.59	Single Cell Mining Claim	4/10/2018	3/21/2025	(100) RIO TINTO EXPLORATION CANADA INC.
187788	21.6	Single Cell Mining Claim	4/10/2018	3/21/2025	(100) RIO TINTO EXPLORATION CANADA INC.
187789	21.6	Single Cell Mining Claim	4/10/2018	3/21/2025	(100) RIO TINTO EXPLORATION CANADA INC.
190635	21.59	Boundary Cell Mining Claim	4/10/2018	3/21/2025	(100) RIO TINTO EXPLORATION CANADA INC.
190636	21.59	Single Cell Mining Claim	4/10/2018	3/21/2025	(100) RIO TINTO EXPLORATION CANADA INC.
190118	21.6	Single Cell Mining Claim	4/10/2018	3/21/2025	(100) RIO TINTO EXPLORATION CANADA INC.
207313	21.6	Single Cell Mining Claim	4/10/2018	3/21/2025	(100) RIO TINTO EXPLORATION CANADA INC.
227913	21.59	Single Cell Mining Claim	4/10/2018	3/21/2025	(100) RIO TINTO EXPLORATION CANADA INC.
254480	21.6	Single Cell Mining Claim	4/10/2018	3/21/2025	(100) RIO TINTO EXPLORATION CANADA INC.
266544	21.6	Single Cell Mining Claim	4/10/2018	3/21/2025	(100) RIO TINTO EXPLORATION CANADA INC.
273298	21.6	Single Cell Mining Claim	4/10/2018	3/21/2025	(100) RIO TINTO EXPLORATION CANADA INC.
294564	21.59	Boundary Cell Mining Claim	4/10/2018	3/21/2025	(100) RIO TINTO EXPLORATION CANADA INC.
303150	21.6	Single Cell Mining Claim	4/10/2018	3/21/2025	(100) RIO TINTO EXPLORATION CANADA INC.
303151	21.6	Single Cell Mining Claim	4/10/2018	3/21/2025	(100) RIO TINTO EXPLORATION CANADA INC.
306672	21.59	Single Cell Mining Claim	4/10/2018	3/21/2025	(100) RIO TINTO EXPLORATION CANADA INC.
320499	21.6	Single Cell Mining Claim	4/10/2018	3/21/2025	(100) RIO TINTO EXPLORATION CANADA INC.
322672	21.6	Single Cell Mining Claim	4/10/2018	3/21/2025	(100) RIO TINTO EXPLORATION CANADA INC.
333731	21.6	Single Cell Mining Claim	4/10/2018	3/21/2025	(100) RIO TINTO EXPLORATION CANADA INC.
333732	21.6	Single Cell Mining Claim	4/10/2018	3/21/2025	(100) RIO TINTO EXPLORATION CANADA INC.
340181	21.59	Single Cell Mining Claim	4/10/2018	4/27/2025	(100) RIO TINTO EXPLORATION CANADA INC.
128672	21.59	Single Cell Mining Claim	4/10/2018	4/27/2025	(100) RIO TINTO EXPLORATION CANADA INC.
128673	21.6	Single Cell Mining Claim	4/10/2018	4/27/2025	(100) RIO TINTO EXPLORATION CANADA INC.
159685	21.6	Single Cell Mining Claim	4/10/2018	4/27/2025	(100) RIO TINTO EXPLORATION CANADA INC.
162626	21.6	Single Cell Mining Claim	4/10/2018	4/27/2025	(100) RIO TINTO EXPLORATION CANADA INC.
225063	21.6	Single Cell Mining Claim	4/10/2018	4/27/2025	(100) RIO TINTO EXPLORATION CANADA INC.
245228	21.6	Single Cell Mining Claim	4/10/2018	4/27/2025	(100) RIO TINTO EXPLORATION CANADA INC.
260422	21.6	Single Cell Mining Claim	4/10/2018	4/27/2025	(100) RIO TINTO EXPLORATION CANADA INC.
269736	21.59	Single Cell Mining Claim	4/10/2018	4/27/2025	(100) RIO TINTO EXPLORATION CANADA INC.
308743	21.6	Single Cell Mining Claim	4/10/2018	4/27/2025	(100) RIO TINTO EXPLORATION CANADA INC.
320486	21.6	Single Cell Mining Claim	4/10/2018	4/27/2025	(100) RIO TINTO EXPLORATION CANADA INC.
267876	21.59	Single Cell Mining Claim	4/10/2018	9/18/2025	(100) RIO TINTO EXPLORATION CANADA INC.

MINING LEASES

CLAIM_NUM	AREA_HECTARES	OWNER	EXPIRY_DATE
109045	15.02	Rio Tinto Exploration Canada Inc.	2033-Feb-28
108872	15.6	Rio Tinto Exploration Canada Inc.	2032-Jul-31
109049	16.11	Rio Tinto Exploration Canada Inc.	2033-Feb-28
108866	13.97	Rio Tinto Exploration Canada Inc.	2031-Mar-31
108870	7.24	Rio Tinto Exploration Canada Inc.	2032-Sep-30
108871	7.01	Rio Tinto Exploration Canada Inc.	2032-Sep-30
108298	14.72	Rio Tinto Exploration Canada Inc.	2029-Nov-30
108874	18.96	Rio Tinto Exploration Canada Inc.	2031-Mar-31
108867	14.01	Rio Tinto Exploration Canada Inc.	2031-Mar-31
108297	16.33	Rio Tinto Exploration Canada Inc.	2029-Nov-30
109044	14.88	Rio Tinto Exploration Canada Inc.	2033-Feb-28
109048	16.53	Rio Tinto Exploration Canada Inc.	2033-Feb-28
108300	17.64	Rio Tinto Exploration Canada Inc.	2029-Nov-30
108873	23.35	Rio Tinto Exploration Canada Inc.	2032-Jul-31
109046	10.68	Rio Tinto Exploration Canada Inc.	2033-Feb-28
108868	16.83	Rio Tinto Exploration Canada Inc.	2032-Sep-30
108875	12.66	Rio Tinto Exploration Canada Inc.	2031-Mar-31
109047	11.15	Rio Tinto Exploration Canada Inc.	2033-Feb-28
108869	4.79	Rio Tinto Exploration Canada Inc.	2032-Sep-30
108294	66.24	Rio Tinto Exploration Canada Inc.	Unknown
108301	63.76	Rio Tinto Exploration Canada Inc.	2029-Nov-30
108293	64.2	Rio Tinto Exploration Canada Inc.	2029-Nov-30
108295	60.35	Rio Tinto Exploration Canada Inc.	2029-Nov-30
108296	32.1	Rio Tinto Exploration Canada Inc.	2029-Nov-30
107289	272.81	Rio Tinto Exploration Canada Inc.	Unknown
107331	94.42	Rio Tinto Exploration Canada Inc.	Unknown
108299	33.18	Rio Tinto Exploration Canada Inc.	Unknown

MINING LAND PATENTS

Tenure Number	Area (Ha)	Owner
PAT-16406	32.38	Rio Tinto Exploration Canada Inc.
PAT-17417	64.75	Rio Tinto Exploration Canada Inc.
PAT-17418	64.75	Rio Tinto Exploration Canada Inc.
PAT-17420	64.75	Rio Tinto Exploration Canada Inc.
PAT-17421	64.75	Rio Tinto Exploration Canada Inc.
PAT-17422	64.75	Rio Tinto Exploration Canada Inc.
PAT-17423	64.75	Rio Tinto Exploration Canada Inc.
PAT-17424	127.07	Rio Tinto Exploration Canada Inc.
PAT-17425	32.38	Rio Tinto Exploration Canada Inc.
PAT-17426	32.38	Rio Tinto Exploration Canada Inc.
PAT-17427	64.75	Rio Tinto Exploration Canada Inc.
PAT-17428	32.78	Rio Tinto Exploration Canada Inc.
PAT-17429	64.75	Rio Tinto Exploration Canada Inc.
PAT-17430	64.75	Rio Tinto Exploration Canada Inc.
PAT-17431	64.75	Rio Tinto Exploration Canada Inc.
PAT-17432	32.38	Rio Tinto Exploration Canada Inc.
PAT-17433	64.75	Rio Tinto Exploration Canada Inc.
PAT-29081	16.19	Rio Tinto Exploration Canada Inc.
PAT-29082	16.19	Rio Tinto Exploration Canada Inc.
PAT-29083	16.19	Rio Tinto Exploration Canada Inc.
PAT-29084	16.19	Rio Tinto Exploration Canada Inc.
PAT-29085	16.19	Rio Tinto Exploration Canada Inc.
PAT-50924	64.75	Rio Tinto Exploration Canada Inc.
PAT-50925	1.92	Rio Tinto Exploration Canada Inc.

4. REGIONAL GEOLOGY

The following is a summary of the Regional Geology of the Midcontinent Rift from O'Brien, 2018.

The western Lake Superior region has had a long geological history recorded in a variety of rock types. These include Archean granites, greenstones, and gneisses of the Superior Province, Paleoproterozoic sedimentary rocks of the Animikie Basin, Mesoproterozoic red-bed sedimentary rocks of the Sibley Group, younger Mesoproterozoic sedimentary, volcanic, and intrusive rocks of the Midcontinent Rift (MCR), and Quaternary glacial deposits. The key geologic terranes specifically related to the Crystal Lake Gabbro (CLG) are the Superior Province, the Animikie Basin, and the MCR. The main geological attributes of these terranes in the western Lake Superior area are described below.

Superior Province

The underlying crust of the MCR is largely the Archean basement of the Superior Province. The Superior Province was developed by the amalgamation of distinct protocontinental and oceanic terranes, that ranged in age between 3.7 and 2.65 Ga, during the accretionary Kenoran Orogeny occurring between 2.72 to 2.68 Ga (Card and Ciesielski, 1986; Percival et al., 2006). The Superior Province is comprised of a series of east-trending belts that are composed of granite-greenstone, metasedimentary, plutonic, and high-grade gneisses and that have been metamorphosed to greenschist-granulite facies (Card and Ciesielski, 1986; Card, 1990). The belts have been subdivided into multiple subprovinces or terranes based on their lithologic, metamorphic, geochemical, isotopic, geochronologic and geophysical characteristics (Card and Ciesielski, 1986; Stott et al., 2010) (Figure 3).

The Wawa subprovince underlies the section of the MCR that hosts the CLG. The Wawa subprovince is the western portion of the Wawa-Abitibi terrane with the Abitibi subprovince comprising the eastern portion, separated by the Kapuskasing structural zone (Stott et al., 2010). The Wawa subprovince is dominantly comprised of large masses of granitoid plutons with isolated arcuate to linear greenstone belts comprising 20 to 30% of the subprovince (Williams et al., 1990).

Animikie Basin

Paleoproterozoic sedimentary rocks of the Animikie Group, which extends through Ontario, Minnesota, Wisconsin, and Michigan, were deposited on Archean crust in a continental shelf/back arc basin about 1.85 Ga (Johnston et al., 2006) (Figure 4). The area of the Animikie Basin intruded by the CLG and Mount Mollie

Dyke (MMD) is termed the Logan Basin. The Animikie Group contains three conformable sedimentary formations: a basal conglomerate/quartzite unit, a chemically precipitated iron formation, and a shale/greywacke formation (Hemming et al., 1995; Fralick et al.,

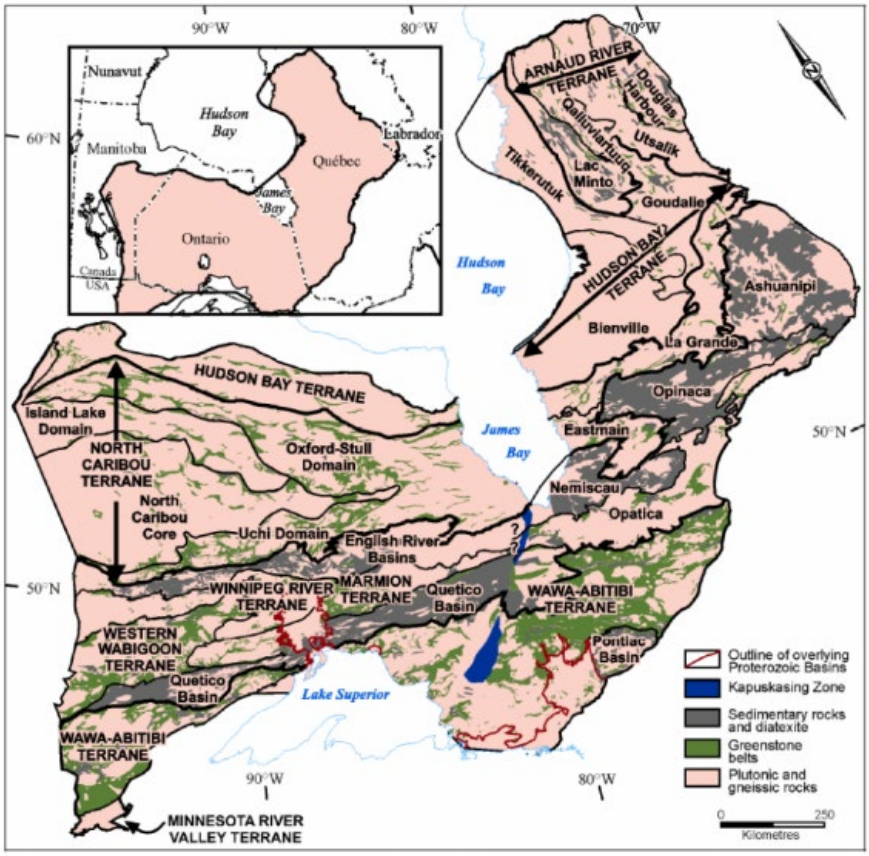

Figure 3: Map of the Archean Superior Province from Stott et al. (2010).

2002; Johnston et al., 2006). The MCR separated the basin into two segments located in Ontario-Minnesota and Wisconsin-Michigan. Local naming of the stratigraphy has occurred over a century of research, although each segment shares similar characteristics and can be correlated with each other; the basal conglomerate/quartzite is known as the Mahnomen, Pokegama, and Kakabeka Formations, the iron formation is known as Trommald, Biwabik and Gunflint Formations, and the shale/grainstone is known as Thompson, Virginia, and Rove Formation (Hemming et al., 1995: Ojakangas et al., 2001). For simplicity Kakabeka, Gunflint, and Rove will be used for the remainder of this document as these are the names most

widely used in the study area.

Development of a passive margin between two land masses on the present southern edge of the Superior Province, was associated with rift development at ~2450 Ma (Johnston et al., 2006). The formation of the passive margin is thought to have occurred in three stages, an intrarift stage, a rift stage, and a post breakup stage (Southwick and Morey, 1991; Ojakangas et al., 2001). Two models have been proposed to explain how the Animikie Basin was formed. One model, outlined in Hoffman (1987), Morey and Southwick (1995), and Ojakangas et al. (2001) suggested that, after initial continental rifting, further development led to the creation of a seafloor which eventually closed as a result of northward subduction and creation of an island arc. This was followed by southward subduction and creation of a volcanic arc, known as the Wisconsin Magmatic Terrane. Eventually complete closure of the ocean occurred with an arc-continent collision.

Due to the collision, a foredeep was created in response to the loading during the Penokean Orogeny, in which the Animikie Group was deposited (Ojakangas et al., 2001). During the evolution of the foredeep there were changes in water depth creating the three formations of the Animikie group; a tidal flat environment where quartzite of the Kakabeka group formed, a shallow water environment where the Gunflint iron formation precipitated and finally to deep-water environment where the turbidites of the Rove Formation formed. The second model, outlined in Bond et al. (1988) for the Cenozoic Aleutian Basin formation and later expanded upon by Pufahl and Fralick (1995), Hemming et al. (1995) and Pufahl et al. (2000), suggests that the Animikie Basin evolved in a back-arc basin which formed as a result of extension created by a northward subduction zone during the sea-floor closure. The back-arc basin was subsequently destroyed by initiation of a fold and thrust belt being formed due to a change in the direction of plate convergence.

Animikie Group in the Logan Basin

Gunflint Formation

The Gunflint Formation hosts one of the most diverse Precambrian fossil communities in the world, including stromatolites with cellular level preservation (Fralick et al., 2002). This formation is 120 to 185 m thick and dips 5 degrees to the south (Goodwin, 1956). Fining and coarsening upward successions found in the formation suggests that there were transgressive and regressive events during deposition (Fralick and Barrett, 1995). The environment during formation was an open and wave dominated shelf where water depth did not exceed 10 m (Pufahl and Fralick, 2004). The chemically precipitated rocks are thought to have

formed by the introduction of iron-rich anoxic bottoms to the oxygenated shelf waters (Pufahl and Fralick, 2004). The Gunflint Formation has been divided into a lower member comprised of stromatolite bioherms, chert-carbonate, grainstones and chemical mud layers and a similar upper member that also contains shales and volcanic ash layers (Fralick et al., 2002). One of the ash layers has an age determined to be 1878 ±1.3 Ma, which is believed to be the age of deposition (Fralick et al., 2002). The upper most portion of the Gunflint Formation contains agate and pyrite veins and vugs, which suggests that after deposition, during the Penokean Orogen (1860 to 1835 Ma) it was subaerially exposed and altered (Johnston et al., 2006). Also, during this hiatus in deposition, an ejecta layer was deposited from the Sudbury Impact which took place 1850 ±1 Ma (Krogh et al., 1984).

Rove Formation

Overlying the Gunflint, a sharp contact defines the bottom of the Rove Formation. The basal section of the Rove Formation consists of black carbonaceous shale with interbedded siltstone and very fine-grained sandstone, with friable tuffaceous layers (Maric and Fralick, 2005). Starting at around 5 m above the basal contact the siltstone and sandstone interlayers become less abundant and are followed by 100 to 150 m of black fissile shale (Maric and Fralick, 2005). This is overlain by a gradational contact to a sequence of over 100 stacked coarsening upward parasequences of a sandstone-shale unit of up to 350 m thickness (Maric and Fralick, 2005). The water depth for these successions is estimated to have been 100 to 200 m (Johnston et al., 2006). The uppermost unit consists of a black shale with wave and current rippled sandstones (Maric and Fralick, 2005). This unit also contains fine-grained and finely dispersed pyrite, suggesting formation in anoxic bottom waters with persistent sulphidic conditions and unrestricted access to open ocean waters (Poulton et al., 2004). The age of deposition was determined by zircons found in the basal and upper units of the Rove Formation that yielded ages of 1835 Ma and 1780 Ma (Heaman, 2005; Addison et al., 2005).

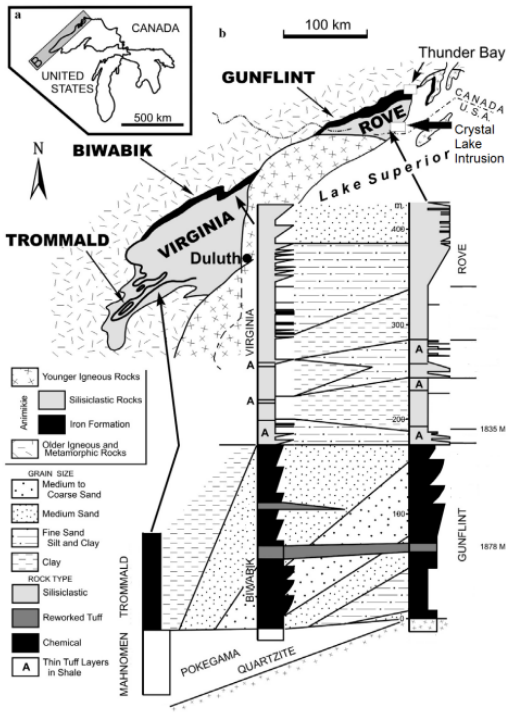

Figure 4: Location, geology and generalized stratigraphy of the Animikie Group. From O'Brien, 2018. Modified from Johnston et al. (2006).

Midcontinent Rift

The Midcontinent Rift (MCR) extends approximately 2500 km from the Grenville front through northwestern Ontario to Kansas (Davis and Green, 1997). It is estimated to contain 1,300,000 km^3 of volcanic and intrusive rocks, although it is difficult to determine an accurate estimate due to loss to erosion, sills, dykes, intrusions still at depth, and magma that has been underplated (Hutchinson et al., 1990; Heaman et al., 2007). The evolution of the MCR started with a broad depression that has a correlated fluvial sequence ~100 m thick at the base of the supracrustal sequence (Ojakangas and Dickas, 2002). Extensive volcanism began around 1100 Ma over a broad area but was ultimately focused into a central graben with approximately 25 km of basalt and lesser rhyolite fill (Cannon, 1992). Around 1086 Ma, extension and volcanism waned and the rift transitioned into a protracted period of subsidence and creation of a sedimentary basin, which was filled by ~8 km of post-rift sediments (Heaman et al., 2007).

The MCR formed from ~1115 to 1084 Ma, with the majority of the igneous activity occurring in two pulses from ~1115 to 1105 Ma and ~1100 to 1094 Ma (Heaman et al., 2007; Vervoort et al., 2007). A plume model

has been suggested and is generally regarded as the most likely scenario for causing the rift, due to the amount and volume of magmatic activity, as well as the isotopic and chemical character of the associated rocks (Hutchinson et al., 1990; Nicholson and Shirey, 1990; Shirey et al.,1994; Nicholson et al., 1997; Shirey, 1997). There are also suggestions that there are some inconsistencies when comparing the MCR to other large igneous provinces (LIPs), largely due to the longer than normal time span of magmatism and lack of an associated radiating dyke swarm (Hollings and Heggie, 2014).

Along the length of the MCR there are a variety of pre-rift rocks into which the intrusions were emplaced. These crustal rocks range in age from 3.6 to 1.5 Ga, with the most voluminous intrusions in Ontario emplaced in the 2.7 Ga crust of the late Archean (Van Schmus, 1992). Hypabyssal rocks dominate the Ontario portion of the MCR related intrusions (Hollings et al., 2010). These intrusions, dykes, and sills are found from the Lake Nipigon area to the Ontario-Minnesota border (Figure 5). These rocks are part of the proposed Logan Igneous Suite and subdivided into two informal groups; the Logan sills south of Thunder Bay and Nipigon sills north of Thunder Bay (Hollings et al., 2007a). Logan sills and Nipigon sills have a uniform paleomagnetic signature but are geochemically distinct from each other (Hollings et al., 2010 and references therein).

MCR Intrusions in the Logan Basin

Logan Sills

The 70 km x 30 km area of the rugged terrane of mesas and ridges towering above flat lying valleys, between Thunder Bay and the Ontario-Minnesota border, was termed the Logan Basin by North (2000). The first published geological map and rock descriptions of the area is that of T. L. Tanton (1931, 1935, and 1936). Further mapping and descriptions of the area was undertaken by Pye and Fenwick (1965), Geul (1970, 1973), and Smith and Sutcliffe (1987, 1989). Whereas the Nipigon sills and intrusions are underlain by the English River, Wabigoon, and Quetico subprovinces of the Superior Province, the Logan Basin is underlain by the Wawa subprovince.

Logan sills were originally classified with the Nipigon Sills based on a similar paleomagnetic signature, but more recently a geochemical difference between the sills north and south of Thunder Bay, has resulted in them being subdivided into two populations (Hollings et al., 2010 and references therein). Sills in the Logan Basin area have higher TiO_2 and more depleted heavy rare earth elements (HREE) than the Nipigon Sills

(Hollings et al., 2007a). The sills are mainly composed of equigranular tholeiitic diabase with chill zones at the contact with the sedimentary rocks of the Animikie Group. From the contact the sills grade upward to fine-grained ophitic diabase, medium-grained megacrystic plagioclase phyric diabase, and an iron-rich diabase which is usually found at surface (Smith and Sutcliffe, 1987). Bulk compositions of the sills are equivalent to an iron-rich quartz tholeiite basalt (Hollings et al., 2010). Thicker sills in the area may contain coarse grained gabbro with granophyre in the interior of the sills (Hollings et al., 2010). The flat lying Rove Formation, into which most of the sills are emplaced, is the main control on the thickness and morphology, often capping mesas and cuestas in the area (Cundari, 2012). Heaman et al. (2007) determined a U-Pb baddeleyite age of 1114.7 ±1.1 Ma for a Logan Sill within the basin.

Logan Basin Dykes

Three suites have been recognized in the Logan basin; the Pigeon River dykes, Cloud River dykes, and the Mount Mollie Dyke (MMD), they are classified mainly by their orientation and age (Cundari, 2012).

Pigeon River dykes trend east-northeast to northeast, dip steeply to the southeast, and are the most abundant in the area. These dykes are thought to have followed preexisting normal faults, as suggested by warping of the Rove Formation on the southern sides of the dykes and slickensides on some contacts that suggests further reactivation of the faults (Smith and Sutcliffe, 1989). The observed contacts of the dykes and Rove Formation are either < 5 cm aphanitic to fine-grained diabase chill zones or 0.5 m to 1 m thick gradational contacts of fine- to medium-grained diorite containing xenoliths of Rove Formation (Smith and Sutcliffe, 1989). Most commonly the rocks are fine- to medium-grained ophitic diabase with oikocrystic clinopyroxene and glomeroporphyritic plagioclase, with a typical mineral assemblage of 60% plagioclase, 20% augite ±hypersthene, up to 15% olivine and up to 5% magnetite, and trace ilmeno-magnetite and sulphides (Geul 1973; Smith and Sutcliffe, 1989). The Pigeon River dykes range in thickness from an average of 50 m to 70 m and up to 150 m, and extend for up to 15 km. Two U-Pb baddeleyite ages have been determined for the Pigeon River dykes 1141 ±20 Ma and 1078 ±4 Ma (Heaman et al., 2007).

Cloud River dykes trend northwest and consist mainly of plagioclase-phyric quartz diabase with a U-Pb baddeleyite age of 1109.3 ±4.2 Ma (Hollings et al., 2010). Inconsistent and contradicting paleomagnetic signatures have also been reported for the Cloud River dykes with Piispa et al. (2011) reporting a N polarity

and Hollings et al. (2010) reporting a R polarity, where the N polarity is more likely due to a higher sample size.

Extending east from the Crystal Lake Gabbro (CLG) lies the 35 km long 60 to 350 m wide MMD which dips between near vertically to 35° North (Geul, 1973). The MMD extends into a series of islands in Lake Superior where it shows a northeast trend compared to the east trend on the mainland. The MMD is a composite dyke with a variety of rock types and textures. Variations in modal mineralogy result in rock types ranging from olivine gabbro to gabbro to hornblende diorite to granophyre. Grain size within the dyke varies from fine to coarse-grained to locally pegmatitic patches. Though typically massive, locally the gabbros display foliation and modal layering (Smith and Sutcliffe, 1989). With increasing quartz and hornblende in the core of the dyke, the gabbro grades into a fine- to coarse-grained diorite with either gradational or sharp contacts with a fine- to medium-grained granophyre (Smith and Sutcliffe, 1989). Smith and Sutcliffe (1989) also note textural evidence for magma mixing of mafic and felsic magmas as noted by apophyses and net veining of granophyre within the diorite and gabbro.

Geul (1970, 1973) and Cundari (2012) have mapped this area to determine relationships between the dyke sets. Based on the cross-cutting relationships as well as textural similarities found in outcrop, Cundari (2012) proposed that the emplacement sequence of the dykes was likely Pigeon River followed by Cloud River and lastly Mount Mollie. Recent geochronological, geochemical, and paleomagnetic studies have attempted to understand the evolution of the dyke sets (Hollings et al., 2007a, 2010, 2012; Heaman et al., 2007; Piispa et al., 2011), though contradictions in geochronology and paleomagnetism still exist.

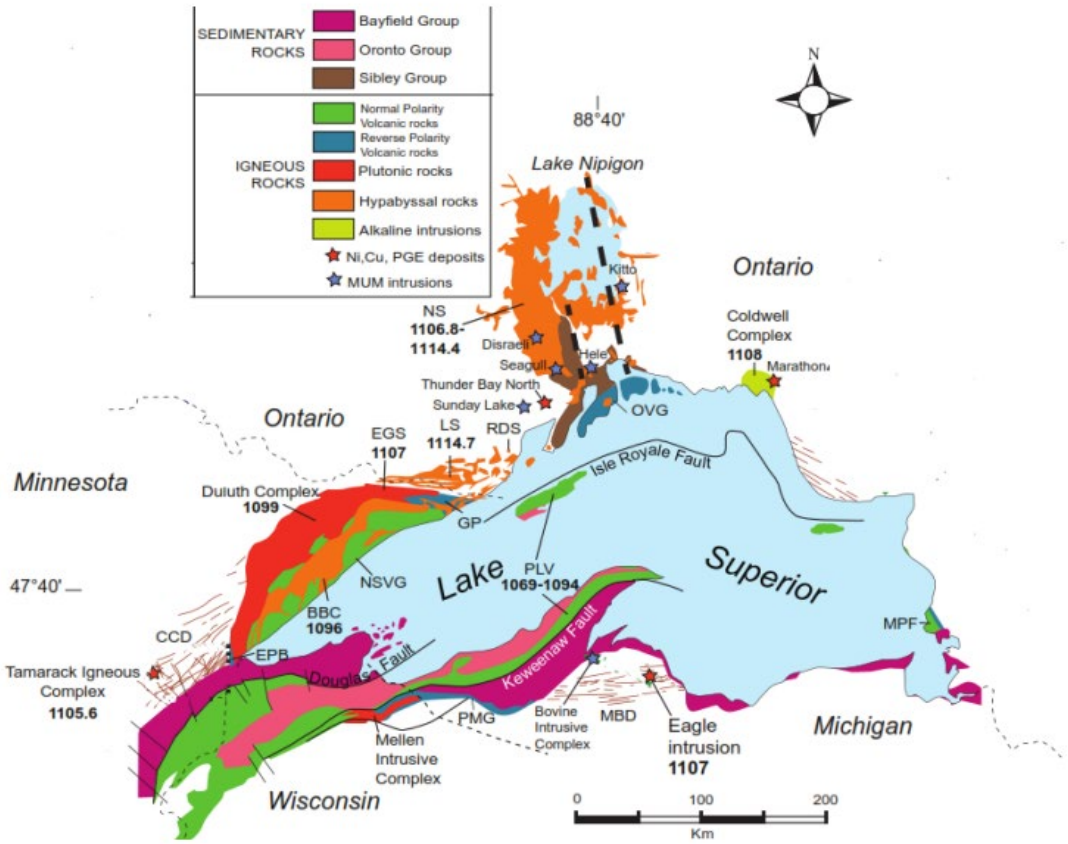

Figure 5: Generalized map of MCR related rocks from O'Brien, 2018. Modified from Paces and Miller (1993) and Miller (pers. comm.) Abbreviations: EGS- Early Gabbro Series; BBC-Beaver Bay Complex; NSVG-North Shore Volcanic Group; GP-Grand Portage volcanics; EPB- Ely's Peak Basalts

Crystal Lake Gabbro

The CLG is Y-shaped in plan view with a 5 km long northern limb trending east and a 2.75 km long southern arm trending east northeast (Figure 6). Based upon layering, foliation, and surface geometry it is thought to be a tilted canoe shaped body which plunges 15 to 20°, opening to the western end of the intrusion (Smith and Sutcliffe, 1989; Cogulu, 1993a).

Based on field observations of the western portion of the northern limb of the CLG, the intrusion has been subdivided into four zones: Basal, Lower, Middle, and Upper. The base of the intrusion consists of a <7 m thick chilled zone of aphanitic to fine-grained gabbro, with partial assimilated xenoliths of the Rove Formation and oval inclusions of Pigeon River Dyke (Smith and Sutcliffe, 1989). The Lower Zone reaches a maximum thickness of 50 m. The lower part of the zone consists of medium- to coarse-grained gabbro with

patches and blocks of pegmatitic gabbro and leucotrocolite as well as disseminated sulphides (Smith and Sutcliffe, 1989). The upper portion of the Lower Zone consists of coarse-grained to pegmatitic leucogabbro and leucotroctolite with elliptical-shaped segregations rich in disseminated chromite that elongate parallel to layering (Smith and Sutcliffe, 1989). The Middle Zone is 30 m thick and defined by distinct phase layering of anorthosite, olivine leucogabbro, chromite rich anorthosite and melanocratic olivine gabbro. The Upper Zone is 80 m thick, defined by the disappearance of chromite rich layers and consists of coarse-grained olivine gabbro with an overlying medium-grained troctolite (Smith and Sutcliffe, 1989).

Cogulu (1993a) reported a great diversity in the chrome spinels regarding composition, reflecting a complex history of crystallization and re-equilibration during post cumulus reactions. Observed textures suggest that the chrome spinels were the first mineral to crystallize, as a result of magma mixing during influxes of new magma (Cogulu, 1993a). Cogulu (1993b) describes two sulphide populations, both consisting of pyrrhotite, chalcopyrite, cubanite, and pentlandite. The first sulphide population forms massive and disseminated ore and is found in the Basal and Lower Zones and the second population is found in the Middle Zone and forms low grade disseminated sulphides (Cogulu, 1993b). The Se/S ratios and sulphur isotopes suggest that assimilation and devolatilization of the sulphidic Rove Formation was the principal source of Cu-Ni mineralization, which was generated from a segregation of a Fe-Ni rich monosulphide solid solution (mss) and later, through fractional crystallization, a Cu rich intermediate solid solution (iss; Cogulu, 1993b; Thomas, 2015).

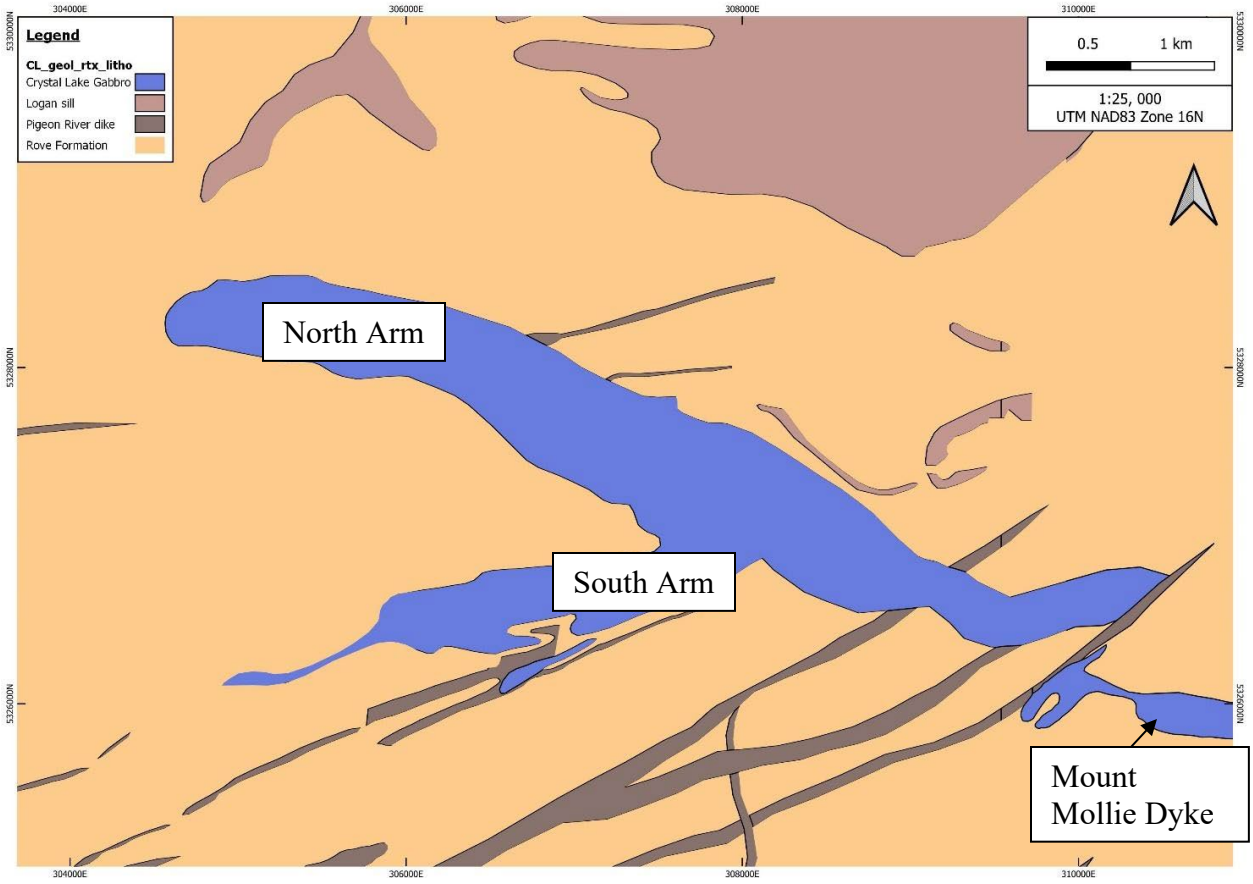

Figure 6: Illustration of the Crystal Lake Gabbro and surrounding geology.

5. AIRBORNE GRAVITY GRADIOMETER AND MAGNETOMETER SURVEY RESULTS

Sampling Procedures & QA/QC

Refer to Appendix A for the Xcalibur Multiphysics logistics and processing report which outlines the sampling procedures and QA/QC undertaken on the Crystal Lake Project.

Results: Airborne Gravity Gradiometer and Magnetometer Survey

The AGG and magnetometer survey was carried out between March 28th and April 2nd , 2022. A total of five production flights were flown over the survey area of 964 kilometers with traverse line spacing of 200 by 100 meters, tie line spacing of 2,000 meters and minimum drape height of 35 meters. Of the 964 line km's of survey data acquired, 602.85 line km's were flown over RTEC mineral tenure. A map showing flight lines and tenure is provided in Appendix B and a breakdown of line km's per tenure ia given in Section 7 of this report. The processing of the HeliFALCON® AGG and aeromagnetic data is summarized in the flow chart in Figure 8 and Figure 12 of Appendix A respectively. Ground surface elevation was obtained by combining

scanner range and angle data with helicopter position and altitude data. The laser scanner data records at the rate of 36 scans per second. Each scan returned 276 data points which was then converted.
The airborne gravity gradient data was obtained using the Fourier domain transformation method which was conformed to the regional data by adding filters grids offering uniform frequency response across overlapping frequencies (Figure 7 or Figure 11 in Appendix A). The first vertical derivative of the final magnetic intensity is shown below. (Figure 8 or Figure 14 in Appendix A).

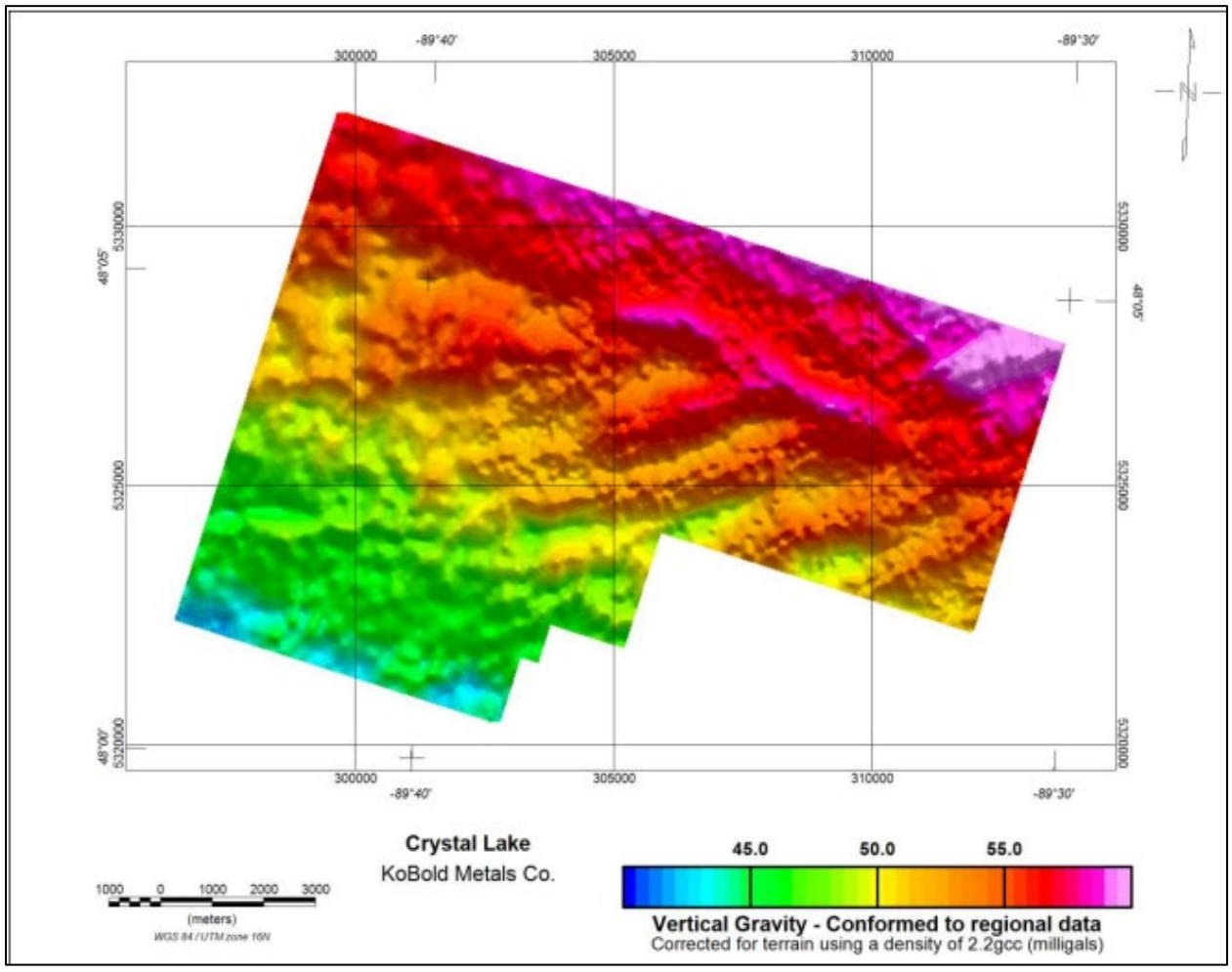

Figure 7:Crystal Lake-Enhanced Vertical Gradient (gD) conformed to regional gravity data.

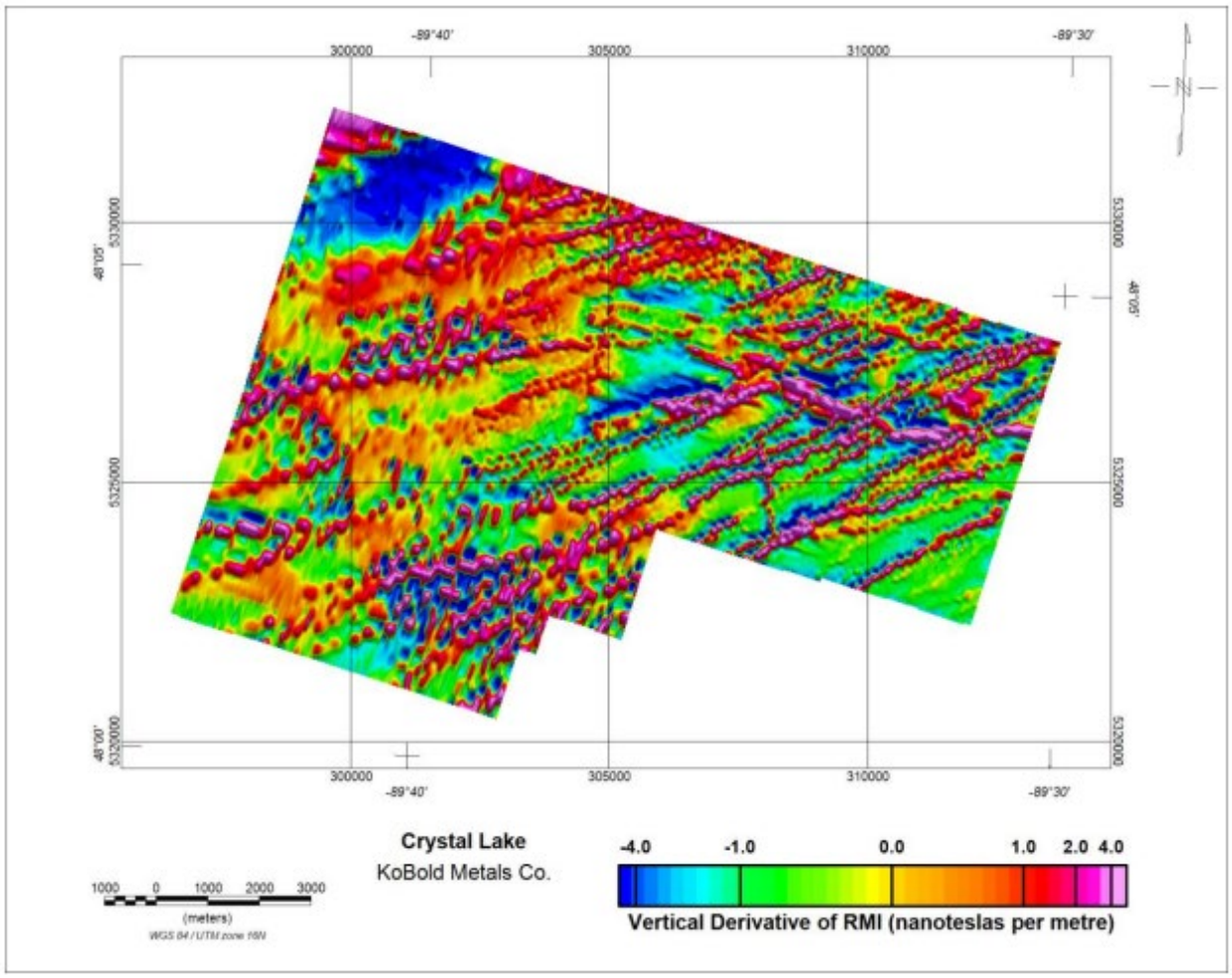

Figure 8:Crystal Lake-First Vertical Derivative of the Final Magnetic Intensity (nT/m)

6. CONCLUSIONS

The HeliFalcon Airborne Gravity Gradiometer and Magnetic surveys provided high resolution data of the Crystal lake Property. The Crystal Lake Gabbro is apparent in both surveys; as a relatively strong positive gravity anomaly and as a more subtle magnetic anomaly that appears to cross cut regional gabbroic dykes.

The data collected from both surveys will be utilized in Duffy Lake's proprietary stochastic inversion model with the intent of generating targets both within the Crystal Lake Gabbro, and elsewhere on the property. Follow up work will include diamond drilling to test high priority targets for massive sulfide accumulation.

7. STATEMENT OF EXPENDITURES

Expenditures for the HeliFALCON AGG and Aeromagnetic survey totaled $401,300. A breakdown of the distribution of those expenditures is presented in the table below. The allocation of expenses to each cell were calculated by determining the total line kilometers that were surveyed over each claim, patent and lease to calculate a proportion of the total spend.

Tenure ID	Length (km)	Proportion	Cost Proportion
104607	2.19	0.36%	$1,456.12
104608	2.67	0.44%	$1,778.42
104609	2.60	0.43%	$1,733.63
104972	1.01	0.17%	$673.97
107491	2.12	0.35%	$1,413.46
108756	2.17	0.36%	$1,445.52
109074	2.16	0.36%	$1,441.06
109190	0.98	0.16%	$654.93
110051	1.62	0.27%	$1,079.48
114018	2.68	0.44%	$1,785.12
118559	2.76	0.46%	$1,833.91
119253	2.17	0.36%	$1,442.72
122207	2.21	0.37%	$1,472.43
122961	2.52	0.42%	$1,674.75
124539	1.61	0.27%	$1,069.33
124540	1.59	0.26%	$1,060.83
124541	1.46	0.24%	$972.82
124542	1.03	0.17%	$685.42
125472	2.11	0.35%	$1,407.72
125473	2.46	0.41%	$1,640.09
126646	1.14	0.19%	$761.21
126647	1.47	0.24%	$980.57
127694	2.21	0.37%	$1,472.45
128099	2.11	0.35%	$1,405.15
128615	1.11	0.18%	$742.07
128672	0.97	0.16%	$644.83
128673	1.14	0.19%	$760.79
131292	2.58	0.43%	$1,717.78
132227	2.22	0.37%	$1,474.82
133926	2.21	0.37%	$1,474.37
135111	1.63	0.27%	$1,081.92
136010	1.15	0.19%	$762.26
137462	2.64	0.44%	$1,759.08
138105	1.14	0.19%	$757.50
138106	0.97	0.16%	$644.75
138126	1.15	0.19%	$762.60
139023	1.07	0.18%	$709.98
139024	1.14	0.19%	$759.83
140641	0.99	0.16%	$656.18
142961	2.19	0.36%	$1,460.52
142962	2.54	0.42%	$1,693.95
143621	1.10	0.18%	$730.30
145021	1.16	0.19%	$771.98
146595	1.14	0.19%	$760.09
152427	1.14	0.19%	$759.13
155185	1.15	0.19%	$763.11
156493	2.12	0.35%	$1,410.69
157720	2.14	0.35%	$1,423.39
159615	2.59	0.43%	$1,725.21
159685	1.58	0.26%	$1,051.76
161399	2.65	0.44%	$1,763.12
162626	1.12	0.19%	$743.70
163807	2.19	0.36%	$1,456.11
165465	1.78	0.30%	$1,186.20
165466	0.97	0.16%	$644.99
167469	1.54	0.25%	$1,022.14
167767	2.18	0.36%	$1,448.70
171173	1.58	0.26%	$1,054.49
172290	2.17	0.36%	$1,447.50
172291	2.11	0.35%	$1,407.32
173319	1.07	0.18%	$709.76
174536	2.66	0.44%	$1,771.01
176272	1.59	0.26%	$1,058.40
177209	2.55	0.42%	$1,695.69
178919	2.11	0.35%	$1,404.83
181619	3.06	0.51%	$2,034.48
181979	1.45	0.24%	$964.99
181980	1.39	0.23%	$926.72
187788	1.03	0.17%	$683.55
187789	1.77	0.29%	$1,178.70
190118	1.14	0.19%	$759.41
190566	4.43	0.74%	$2,950.42
190635	1.47	0.24%	$976.58
190636	1.14	0.19%	$761.26
191640	1.14	0.19%	$760.47
192101	2.64	0.44%	$1,755.99
192161	2.11	0.35%	$1,406.90
194742	1.14	0.19%	$760.77
197004	2.33	0.39%	$1,551.32
198516	3.07	0.51%	$2,041.84
199792	1.08	0.18%	$719.85
204745	1.62	0.27%	$1,081.58
205482	2.56	0.43%	$1,707.02
205837	2.11	0.35%	$1,404.63
207313	1.52	0.25%	$1,012.43
208449	2.67	0.44%	$1,780.60
209056	2.11	0.35%	$1,407.36
209057	2.63	0.44%	$1,750.46
211119	0.97	0.16%	$644.43
211120	1.43	0.24%	$953.58
213289	1.05	0.17%	$701.46
213752	2.34	0.39%	$1,560.37
214353	1.03	0.17%	$682.59
215577	2.21	0.37%	$1,471.90
218833	2.11	0.35%	$1,405.74
220485	2.60	0.43%	$1,729.94
223095	2.11	0.35%	$1,407.08
224503	2.16	0.36%	$1,438.85
224839	1.46	0.24%	$974.76
225063	1.01	0.17%	$675.17
227913	1.14	0.19%	$759.84
228474	2.34	0.39%	$1,557.05
229329	1.33	0.22%	$888.28
232744	2.11	0.35%	$1,404.63
234743	2.65	0.44%	$1,760.84
234744	2.65	0.44%	$1,761.04
235869	1.61	0.27%	$1,069.38
239765	1.43	0.24%	$952.90

Tenure ID	Length (km)	Proportion	Cost Proportion
242016	3.04	0.50%	$2,021.25
243263	2.70	0.45%	$1,795.42
243264	2.11	0.35%	$1,407.31
245228	1.00	0.17%	$662.54
245608	2.22	0.37%	$1,474.96
248840	1.10	0.18%	$731.18
249845	1.47	0.24%	$976.58
250033	2.16	0.36%	$1,440.01
251665	2.17	0.36%	$1,441.87
252260	1.45	0.24%	$965.47
252261	1.54	0.26%	$1,024.64
253674	2.59	0.43%	$1,725.46
253675	2.11	0.35%	$1,404.51
254413	2.01	0.33%	$1,336.30
254480	1.45	0.24%	$963.02
260422	1.71	0.28%	$1,140.14
260509	1.14	0.19%	$761.09
263663	2.16	0.36%	$1,438.57
263678	2.13	0.35%	$1,415.74
263765	1.66	0.27%	$1,102.08
263766	1.14	0.19%	$760.73
264022	2.11	0.35%	$1,405.23
266544	1.43	0.24%	$953.57
267876	1.62	0.27%	$1,080.66
268588	1.15	0.19%	$763.11
268712	1.09	0.18%	$727.15
269465	2.21	0.37%	$1,474.41
269736	1.92	0.32%	$1,275.05
270744	1.15	0.19%	$762.28
271478	2.11	0.35%	$1,405.43
273298	1.14	0.19%	$761.19
274461	3.15	0.52%	$2,096.85
275699	2.46	0.41%	$1,638.55
278308	2.15	0.36%	$1,433.99
279075	2.14	0.35%	$1,423.15
279076	2.57	0.43%	$1,713.32
279077	2.68	0.44%	$1,781.01
280458	2.21	0.37%	$1,471.33
280459	2.19	0.36%	$1,460.42
280745	1.62	0.27%	$1,080.82
282850	2.19	0.36%	$1,454.54
290608	2.16	0.36%	$1,435.96
291891	1.55	0.26%	$1,032.51
292774	2.20	0.36%	$1,461.56
294564	1.59	0.26%	$1,058.40
299132	2.52	0.42%	$1,677.20
299133	2.13	0.35%	$1,417.55
299368	1.09	0.18%	$722.43
299690	2.11	0.35%	$1,405.28
300577	1.06	0.18%	$704.58
303150	1.61	0.27%	$1,069.61
303151	0.97	0.16%	$645.07
304579	1.71	0.28%	$1,135.19
305445	2.20	0.37%	$1,465.86

Tenure ID	Length (km)	Proportion	Cost Proportion
306672	1.05	0.17%	$696.33
307078	1.14	0.19%	$759.74
307079	1.14	0.19%	$759.31
308689	2.48	0.41%	$1,647.63
308690	1.00	0.17%	$662.95
308743	1.14	0.19%	$761.47
309103	0.97	0.16%	$648.24
309135	2.13	0.35%	$1,418.13
309136	2.16	0.36%	$1,439.58
310307	2.09	0.35%	$1,390.07
310308	1.14	0.19%	$760.29
312196	2.22	0.37%	$1,475.49
314869	2.17	0.36%	$1,445.36
315868	2.38	0.40%	$1,586.89
315869	1.02	0.17%	$678.53
318300	2.11	0.35%	$1,404.99
318564	2.49	0.41%	$1,660.79
319662	2.12	0.35%	$1,411.78
319663	2.20	0.37%	$1,466.59
320486	1.13	0.19%	$752.06
320499	1.57	0.26%	$1,045.71
322672	1.59	0.26%	$1,058.53
323833	2.55	0.42%	$1,697.16
324277	3.12	0.52%	$2,077.24
324278	3.58	0.59%	$2,381.49
326337	2.18	0.36%	$1,447.93
327715	2.16	0.36%	$1,435.51
327716	2.70	0.45%	$1,794.07
328635	1.14	0.19%	$761.92
328636	0.97	0.16%	$644.96
330684	1.14	0.19%	$761.58
331454	2.11	0.35%	$1,405.48
332141	1.14	0.19%	$760.91
333210	2.22	0.37%	$1,474.59
333731	1.06	0.18%	$702.55
333732	0.98	0.16%	$653.86
335223	0.97	0.16%	$648.35
335224	1.54	0.25%	$1,022.79
335735	2.22	0.37%	$1,475.05
335736	2.21	0.37%	$1,473.27
338725	2.68	0.44%	$1,783.32
338726	2.16	0.36%	$1,434.57
340181	1.14	0.19%	$761.44
343456	1.04	0.17%	$693.51
344349	1.15	0.19%	$763.70
503170	1.63	0.27%	$1,083.36
503171	1.51	0.25%	$1,006.05
503172	1.07	0.18%	$709.37
503173	1.14	0.19%	$760.30
503174	1.45	0.24%	$965.63
503175	1.14	0.19%	$756.79
503176	1.51	0.25%	$1,002.39
503177	1.43	0.24%	$952.68
503178	1.14	0.19%	$760.40

Tenure ID	Length (km)	Proportion	Cost Proportion
503179	1.08	0.18%	$716.03
503180	1.52	0.25%	$1,011.38
503181	1.15	0.19%	$762.68
503182	2.07	0.34%	$1,375.09
503183	1.61	0.27%	$1,069.77
503184	1.43	0.24%	$954.28
503185	1.61	0.27%	$1,069.13
503186	1.01	0.17%	$669.17
503187	1.39	0.23%	$923.41
639535	2.11	0.35%	$1,406.64
PAT-16406	3.38	0.56%	$2,249.20
PAT-17417	5.89	0.98%	$3,918.97
PAT-17418	3.84	0.64%	$2,553.77
PAT-17420	6.29	1.04%	$4,186.11
PAT-17421	5.91	0.98%	$3,934.93
PAT-17422	5.79	0.96%	$3,854.17
PAT-17423	6.34	1.05%	$4,221.68
PAT-17424	12.85	2.13%	$8,551.53
PAT-17425	4.07	0.67%	$2,707.88
PAT-17426	4.61	0.76%	$3,069.04
PAT-17427	4.52	0.75%	$3,011.07
PAT-17428	3.72	0.62%	$2,479.48
PAT-17429	3.42	0.57%	$2,278.02
PAT-17430	7.07	1.17%	$4,706.57
PAT-17431	6.82	1.13%	$4,539.67
PAT-17432	3.28	0.54%	$2,185.41
PAT-17433	6.19	1.03%	$4,123.01
PAT-29081	0.96	0.16%	$638.48
PAT-29082	0.86	0.14%	$569.46
PAT-29083	0.93	0.15%	$617.30
PAT-29084	0.81	0.13%	$540.97
PAT-29085	1.00	0.17%	$663.01
PAT-50924	2.66	0.44%	$1,770.96
PAT-50925	0.30	0.05%	$201.60
107289	28.24	4.68%	$18,796.79
107331	9.75	1.62%	$6,486.99
108293	6.97	1.16%	$4,640.27
108294	6.76	1.12%	$4,503.05
108295	6.31	1.05%	$4,199.91
108296	3.62	0.60%	$2,409.57
108297	1.63	0.27%	$1,085.10
108298	1.48	0.25%	$984.28
108300	1.78	0.29%	$1,181.56
108301	6.40	1.06%	$4,263.22
108866	1.42	0.24%	$947.36
108867	1.46	0.24%	$968.62
108868	1.95	0.32%	$1,301.16
108869	0.42	0.07%	$279.99
108870	0.84	0.14%	$558.89
108871	0.69	0.11%	$457.93
108872	1.55	0.26%	$1,032.43
108873	2.57	0.43%	$1,709.41
108874	2.32	0.38%	$1,542.57
108875	1.24	0.21%	$823.64

Tenure ID	Length (km)	Proportion	Cost Proportion
109044	1.49	0.25%	$988.85
109045	1.50	0.25%	$997.33
109046	1.06	0.18%	$705.38
109047	1.11	0.18%	$740.40
109048	1.71	0.28%	$1,136.41
109049	1.61	0.27%	$1,073.10
Total	***602.85***	***100.00%***	***$401,300.00***

8. SIGNATURES

I, Steven D. Flank, of the City of Thunder Bay, in the Province of Ontario, do hereby certify that:

1. I am the President and Principal Geoscientist of Bayside Geoscience Inc., a geological consulting company based in Thunder Bay, Ontario.
2. I am a member in good standing with the Association of Professional Geoscientists of Ontario (#2695), residing at 124 Sherwood Drive, Thunder Bay, Ontario, P7B 6L1.
3. I attained an H.BSc. in Geology from Lakehead University in Thunder Bay, Ontario (2011) and an M.Sc. in Mineral Exploration from Laurentian University in Sudbury, Ontario (2017).
4. I have worked as an exploration geologist for over 11 years focusing on project generation and early-stage gold projects including shear zone hosted lode gold and intrusion related disseminated gold deposits and intrusion related Ni-Cu-PGE deposits.
5. I have personally reviewed all technical elements of the 2021-2022 Borehole and Fixed Loop TEM Survey and am the signing author of this report.

Dated

March 21, 2023

Thunder Bay, Ontario, Canada

Steven D. Flank, M.Sc., P.Geo.

9. REFERENCES

Addison, W.D., Brumpton, G.R., Vallini, D.A., McNaughton, N.J., Davis, D.W., Kissin, S.A., Fralick, P.W. and Hammond, A.L. (2005) Discovery of distal ejecta from the 1850 Ma Sudbury impact event. Geology 33, 193-196.

Bond, G. C., Lewis, S. D., Taber, J., Steckler, M. S. and Kominz, M. A. (1988) Evidence for formation of a flexural backarc basin by compression and crustal thickening in the central Alaska Peninsula. Geology 16, 1147-1150.

Cannon, W.F. (1992) The Midcontinent rift in the Lake Superior region with emphasis on its geodynamic evolution. Tectonophysics 213, 41-48.

Card, K. and Ciesielski, A. (1986) Subdivisions of the Superior Province of the Canadian shield. Geoscience Canada 13, 5-13.

Card, K. (1990) A review of the Superior Province of the Canadian Shield, a product of Archean accretion. Precambrian Research 48, 99-156.

Cogulu, E. (1993a) Factors controlling postcumulus compositional changes of chromespinels in the Crystal Lake intrusion, Thunder Bay, Ontario. Geological Survey of Canada, Open File 2748, 28.

Cogulu, E. (1993b) Mineralogy and chemical variations of sulphides from the Crystal Lake intrusion, Thunder Bay, Ontario. Geological Survey of Canada, Open File 2749, 21.

Cundari, R. (2012) Geology and geochemistry of Midcontinent Rift-related igneous rocks; unpublished M. Sc thesis, Lakehead University, Thunder Bay, Ontario, 153p.

Davis, D. and Green, J. (1997) Geochronology of the North American Midcontinent rift in western Lake Superior and implications for its geodynamic evolution. Canadian Journal of Earth Sciences 34, 476-488.

Fralick, P.W. and Barrett, T.J. (1995). Depositional controls on iron formATion association in Canada. Sedimentary facies analysis. International Association of Sedimentologists, Special Publication No. 22, 35-39.

Fralick, P., Davis, D.W. and Kissin, S.A. (2002) The age of the Gunflint Formation, Ontario, Canada: single zircon U–Pb age determinations from reworked volcanic ash. Canadian Journal of Earth Sciences 39, 1085-1091.

Geul, J. (1970) Devon and Pardee townships and the Stuart location. Ontario DEPARTMENT of Mines. Geological Report 87, 31-41.

Geul, J. (1973) Geology of Crooks Township, Jarvis and Prince Locations, and Off-shore Islands, District of Thunder Bay. Ontario Department of Mines Geological Report 102, 46.

Goodwin, A.M. (1956) Facies relations in the Gunflint iron formation [Ontario]. Economic Geology 51, 565-595.

Heaman, L., Easton, R., Hart, T., MacDonald, C., Fralick, P. and Hollings, P. (2005) Proterozoic history of the Lake Nipigon area, Ontario: constraints from U–Pb zircon and baddeleyite dating, Ontario Exploration and Geoscience Symposium, Abstract 162 Volume. Ontario Prospectors Association and Northern Ontario Heritage Fund, Toronto, 12-14.

Heaman, L., Easton, R., Hart, T., Hollings, P., MacDonald, C. and Smyk, M. (2007) Further refinement to the timing of Mesoproterozoic magmatism, Lake Nipigon region, Ontario. Canadian Journal of Earth Sciences 44, 1055-1086.

Hemming, S., McLennan, S. and Hanson, G. (1995) Geochemical and Nd/Pb isotopic evidence for the provenance of the Early Proterozoic Virginia Formation, Minnesota. Implications for the tectonic setting of the Animikie Basin. The Journal of Geology 103, 147-168.

Hoffman, P.F. (1987) Early Proterozoic Foredeeps, Foredeep Magmatism, and Superior-Type Iron-Formations of the Canadian Shield. Proterozic Lithospheric Evolution, 85-98.

Halls, H. and Pesonen, L. (1982) Paleomagnetism of Keweenawan rocks. Geology and tectonics of the Lake Superior Basin. Geological Society of America, Memoir 156, 165-171.

Hollings, P., Hart, T., Richardson, A. and MacDonald, C.A. (2007a) Geochemistry of the Mesoproterozoic intrusive rocks of the Nipigon Embayment, northwestern Ontario: evaluating the earliest phases of rift development. Canadian Journal of Earth Sciences 44, 1087-1110.

Hollings, P., Smyk, M., Heaman, L.M. and Halls, H. (2010) The geochemistry, geochronology and paleomagnetism of dikes and sills associated with the Mesoproterozoic Midcontinent Rift near Thunder Bay, Ontario, Canada. Precambrian Research 183, 553-571.

Hollings, P., Smyk, M. and Cousens, B. (2012) The radiogenic isotope characteristics of dikes and sills associated with the Mesoproterozoic Midcontinent Rift near Thunder Bay, Ontario, Canada. Precambrian Research 214, 269-279.

Hollings, P. and Heggie, G. (2014) Rethinking the Midcontinent Rift–puncturing the “plume paradigm”. Proceedings, Institute on Lake Superior Geology, 60th, Part 1, 57.

Hutchinson, D., White, R., Cannon, W. and Schulz, K. (1990) Keweenaw hot spot: geophysical evidence for a 1.1 Ga mantle plume beneath the Midcontinent Rift System. Journal of Geophysical Research: Solid Earth 95, 10869-10884.

Johnston, D.T., Poulton, S.W., Fralick, P.W., Wing, B.A., Canfield, D.E. and Farquhar, J. (2006) Evolution of the oceanic sulfur cycle at the end of the Paleoproterozoic. GeochEmica et CosmochEmica Acta 70, 5723-5739.

Maric, M. and Fralick, P. (2005) Sedimentology of the Rove and Virginia Formations and their tectonic significance. Institute of Lake Superior Geology 51, 41-42.

McGoran, J.P (1991), AFRI52A04SW0101, Exploration Program, Isotalo Property, Pardee Township, Thunder Bay Mining Division, Ontario

Morey, G. and Southwick, D. (1995) Allostratigraphic relationships of Early Proterozoic Iron-formations in the Lake Superior region. Economic Geology 90, 1983-1993.

North, J. (2000) Nature and distribution of Logan diabase sills and gabbro channels in the Keweenawan rift near Thunder Bay, Ontario. Brief comparison to Noril'sk. Abstract, 46th Institute on Lake Superior Geology, Annual Meeting, Proceedings, pp. 43-44.

Nicholson, S.W. and Shirey, S.B. (1990) Midcontinent rift volcanism in the Lake Superior region: Sr, Nd, and Pb isotopic evidence for a mantle plume origin. Journal of Geophysical Research: Solid Earth 95, 10851-10868.

Nicholson, S.W., Schulz, K.J., Shirey, S.B. and Green, J.C. (1997) Rift-wide correlation of 1.1 Ga Midcontinent rift system basalts: implications for multiple mantle sources during rift development. Canadian Journal of Earth Sciences 34, 504-520.

Ojakangas, R., Morey, G. and Southwick, D. (2001) Paleoproterozoic basin development and sedimentation in the Lake Superior region, North America. Sedimentary Geology 141, 319-341.

Ojakangas, R.W. and Dickas, A.B. (2002) The 1.1-Ga Midcontinent Rift System, central North America: sedimentology of two deep boreholes, Lake Superior region. Sedimentary Geology 147, 13-36.

Percival, J., Sanborn-Barrie, M., Skulski, T., Stott, G., Helmstaedt, H. and White, D. (2006) Tectonic evolution of the western Superior Province from NATMAP and Lithoprobe studies. Canadian Journal of Earth Sciences 43, 1085-1117.

Pesonen, L. (1978) Paleomagnetic, paleointensity and paleosecular variation studies on Keweenawan igneous and baked contact rocks. Unpublished Ph.D. thesis. University of Toronto, p.346.

Piispa, E., Smirnov, A. and Pesonen, L. (2011) Paleomagnetism of Midcontinent Rift rocks from the northern shore of Lake Superior (Ontario Canada): Preliminary results, Institute on Lake Superior Geology Proceedings, 57th Annual Meeting, Ashland, WI, p. 65.

Poulton, S.W., Fralick, P.W. and Canfield, D.E. (2004) The transition to a sulphidic ocean ~1.84 billion years ago. Nature 431, 173. Pufahl, P. and Fralick, P. (1995) Paleogeographic reconstruction of the Gunflint–Mesabi–Cuyuna depositional system: a basin analysis approach. Proc. Ins. Lake Super. Geol 41, 59-60.

Pufahl, P., Fralick, P. and Scott, J. (2000) Depositional environments of the Paleoproterozoic Gunflint Formation;46th Institute on Lake Superior Geology, v.46, pt.2, Proceedings with abstracts.

Pufahl, P.K. and Fralick, P.W. (2004) Depositional controls on Palaeoproterozoic iron formation accumulation, Gogebic Range, Lake Superior region, USA. Sedimentology 51, 791-808.

Pye, E. and Fenwick, K. (1965) Atikokan-Lakehead Sheet, Kenora, Rainy River and Thunder Bay Districts. Ontario Department of Mines. Geological Compilation Series, Map 2065, scale 1 inch = 4 miles.

Shirey, S.B., Berg, J.H. and Carlson, R.W. (1994) Temporal changes in the sources of flood basalts: isotopic and trace element evidence from the 1100 Ma old Keweenawan Mamainse Point Formation, Ontario, Canada. Geochimica et Cosmochimica ACTA 58, 4475-4490.

Shirey, S.B. (1997) Re-Os isotopic compositions of Midcontinent rift system picrites: implications for plume–lithosphere interaction and enriched mantle sources. Canadian Journal of Earth Sciences 34, 489-503.

Simonson, B.M. and Hassler, S.W. (1996) Was the deposition of large Precambrian iron formations linked to major marine transgressions? The Journal of Geology 104, 665-676.

Smith, A. and Sutcliffe, R. (1987) Keweenawan intrusive rocks of the Thunder Bay area. Summary of field work, 248-255.

Smith, A. and Sutcliffe, R. (1989) Precambrian Geology, Keweenawan Intrusive Rocks in the Crystal Lake-Pigeon River Area. Ontario Geological Survey. Map 3139, scale 1:50 000.

Southwick, D.L., Morey, G.B. and Holst, T.B. (1991) Tectonic imbrication and foredeep development in the Penokean Orogen, east-central Minnesota: an interpretation based on regional geophysics and the results of test-drilling. US Geological Survey, p. 17.

Stott, G., Corkery, M., Percival, J., Simard, M. and Goutier, J. (2010) A revised terrane subdivision of the Superior Province. Ontario Geological Survey, Open File Report 6260, 20-21.

Tanton, T.L. (1931) Fort William and Port Arthur, and Thunder cape map-areas: Thunder BAY district, Ontario. Map 354A, scale 1:63360.

Tanton, T.L. (1935) Pigeon River area, Thunder Bay District. Geological Survey of Canada, Sheet 1. Map 354A, scale 1:63360.

Tanton, T.L. (1936) Pigeon River area, Thunder Bay District. Geological Survey of Canada, Sheet 2. Map 355A, scale 1:63360.

Thomas, B. (2015) Geochemistry, sulfur isotopes, and petrography of the Cu-Ni-PGE mineralized Crystal Lake Intrusion, Thunder Bay, Ontario. Unpublished M.Sc. Thesis, Indiana University, p. 49.

Van Schmus, W. (1992) Tectonic setting of the Midcontinent Rift system. Tectonophysics 213, 1-15.

Vervoort, J.D., Wirth, K., Kennedy, B., Sandland, T. and Harpp, K.S. (2007) The magmatic evolution of the Midcontinent rift: New geochronologic and geochemical evidence from felsic magmatism. Precambrian Research 157, 235-268.

Williams, H., Stott, G., Heather, K., Muir, T. and Sage, R. (1990) Wawa subprovince. Geology of Ontario, Ontario Geological Survey, Special Volume 4, 485-541.

APPENDIX A: XCALIBUR MULTIPHYSICS LOGISTICAL REPORT

KoBold Metals Co.

HeliFALCON™ Airborne Gravity Gradiometer and Magnetometer Survey

Crystal Lake, Ontario

Project Number: 2200072

Logistics and Processing Report

CGG Canada Services Ltd
2505 Meadowvale Boulevard
Mississauga, Ontario, L5N 5S2
CANADA
Tel: +1 (905) 812-0212, Fax: +1 (905) 812-1504

Xcalibur MULTIPHYSICS

Exploring the world
Safer, Clearer, Better

Table of contents

Figures

Tables

1 INTRODUCTION

Xcalibur Multiphysics conducted a high-sensitivity aeromagnetic and **HeliFALCON™** Airborne Gravity Gradiometer (AGG) survey over the Crystal Lake survey area under contract with KoBold Metals Co.

1.1 Survey Location

The Crystal Lake survey area is centred on longitude 89° 36' W, latitude 48º 03' N (see the location map in *Figure 1*). The production flights took place during March and April 2022 with the first production flight taking place on March 28th and the final flight taking place on April 2nd. To complete the survey area coverage a total of 5 production flights were flown.

Figure 1: Crystal Lake – Survey Area Location

1.2 General Disclaimer

It is Xcalibur Multiphysics' understanding that the data and report provided to the Client are to be used for the purpose agreed between the parties. That purpose was a significant factor in determining the scope and level of the Services being offered to the Client. Should the purpose for which the data and report are used change, the data and report may no longer be valid or appropriate and any further use of, or reliance upon, the data and report in those circumstances by the Client without Xcalibur Multiphysics' review and advice shall be at the Client's own and sole risk.

The Services were performed by Xcalibur Multiphysics exclusively for the purposes of the Client. Should the data and report be made available in whole or part to any third party, and such party relies thereon, that party does so wholly at its own and sole risk and Xcalibur Multiphysics disclaims any liability to such party.

Where the Services have involved Xcalibur Multiphysics' use of any information provided by the Client or third parties, upon which Xcalibur Multiphysics was reasonably entitled to rely, then the Services are limited by the accuracy of such information. Xcalibur Multiphysics is not liable for any inaccuracies (including any incompleteness) in the said information, save as otherwise provided in the terms of the contract between the Client and Xcalibur Multiphysics.

2 SUMMARY OF SURVEY PARAMETER

2.1 Survey Area Specifications

Total Kilometres (km)	964
Clearance Method	Terrain Clearance
Minimum Drape Height (m)	35
Traverse Line Direction (deg.)	108 / 288
Traverse Line Spacing (m)	200 / 100
Tie Line Direction (deg.)	18 / 198
Tie Line Spacing (m)	2000

Table 1: Crystal Lake – Specifications

The survey block is defined by the coordinates in *Table 2*, in UTM Zone 16N projection, referenced to the WGS84 datum.

Corner Number	Easting	Northing
1	296512	5322424
2	299671	5332267
3	313753	5327747
4	311964	5322173
5	305916	5324114
6	305201	5321885
7	303787	5322338
8	303549	5321595
9	303212	5321703
10	302796	5320407

Table 2: Crystal Lake – Survey Boundary Coordinates

2.2 Data Recording

The following parameters were recorded during the course of the survey:

- **HeliFALCON™ AGG data:** recorded at different intervals.
- **Airborne total magnetic field:** recorded with a 0.1 s sampling rate.
- **Terrain clearance:** provided by the radar altimeter at intervals of 0.1 s.
- **Airborne GPS positional data** (latitude, longitude, height, time and raw range from each satellite being tracked): recorded at intervals of 1 s.
- **Time markers:** in digital data.
- **Ground total magnetic field:** recorded with a 1 s sampling rate.
- **Ground based GPS positional data** (latitude, longitude, height, time and raw range from each satellite being tracked): recorded at intervals of 1 s.
- **Ground surface below helicopter:** mapped by the laser scanner system (when within range of the instrument and in the absence of thick vegetation), scanning at 36 times per second, recording 276 returns per scan.

3 FIELD OPERATIONS

3.1 Operations

The survey was based out of Thunder Bay, Ontario. The helicopter was operated from airport using aviation fuel available on site. A temporary office was set up in Thunder Bay where all survey operations were run, and the post-flight data verification was performed.

3.2 Base Stations

A dual frequency GPS base station was set up at the Thunder Bay Airport in order to correct the raw GPS data collected in the helicopter. A secondary GPS base station was available but was not required.

3.2.1 GPS Base Station

Location: GPS base (ITRF 2014)

Date: March 28th, 2022

Latitude: 48º 22' 16.611" N

Longitude: 89º 18' 57.266" W

Height: 159.45 m ellipsoidal

3.2.2 Magnetometer Base Station (CF1)

Location: MAG base

Date: March 28th, 2022

Used for flights: All flights

Base: 55700 nT

3.3 Field Personnel

The following technical personnel participated in field operations:

Crew Leader:	A. Malik
Pilots:	J. Kitchen
LAME/AME:	D. Grant
Technicians:	A. Malik, M.Owen
Project Manager:	A. Heydorn
QC and Processing:	M. Deane, C. van Galder

Table 3: Crystal Lake – Field Personnel

4 QUALITY CONTROL RESULTS

4.1 Survey acquisition issues

During the course of the survey, there were no data quality issues with:

- AGG instrumentation
- Magnetic and GPS base stations
- Airborne magnetometer system
- Data acquisition systems
- Radar altimeter
- Laser scanner

4.2 Flight Path Map

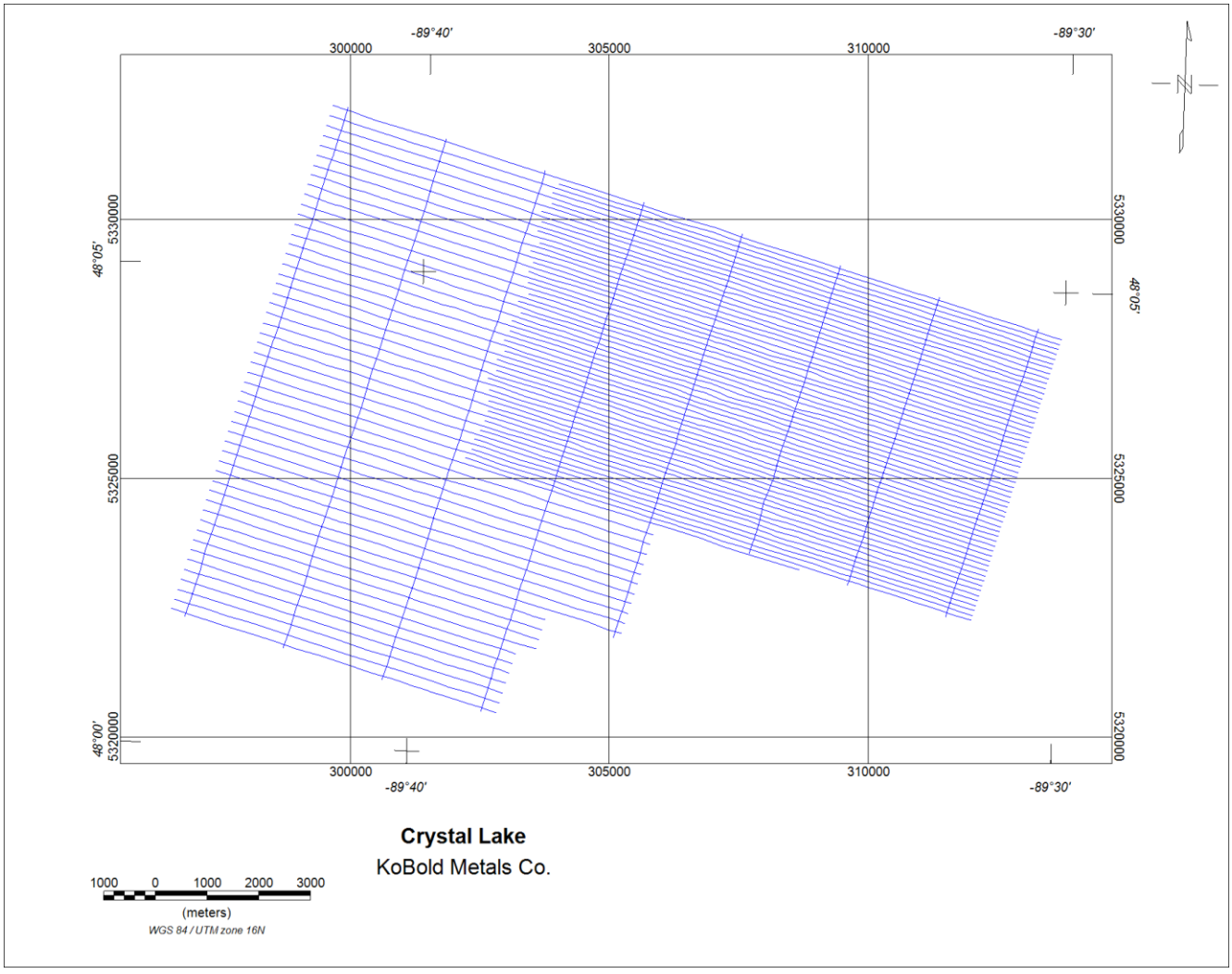

Figure 2: Crystal Lake – Flight Path map

4.3 Turbulence

The mean turbulence recorded was 37.0 milli g (where g = 9.80665 m/sec/sec). Turbulence was variable, ranging from very low to high. The typical pattern for a given flight was for turbulence to commence at a very low level and then increase throughout the flight. The turbulence pattern across the survey area is shown in *Figure 3*.

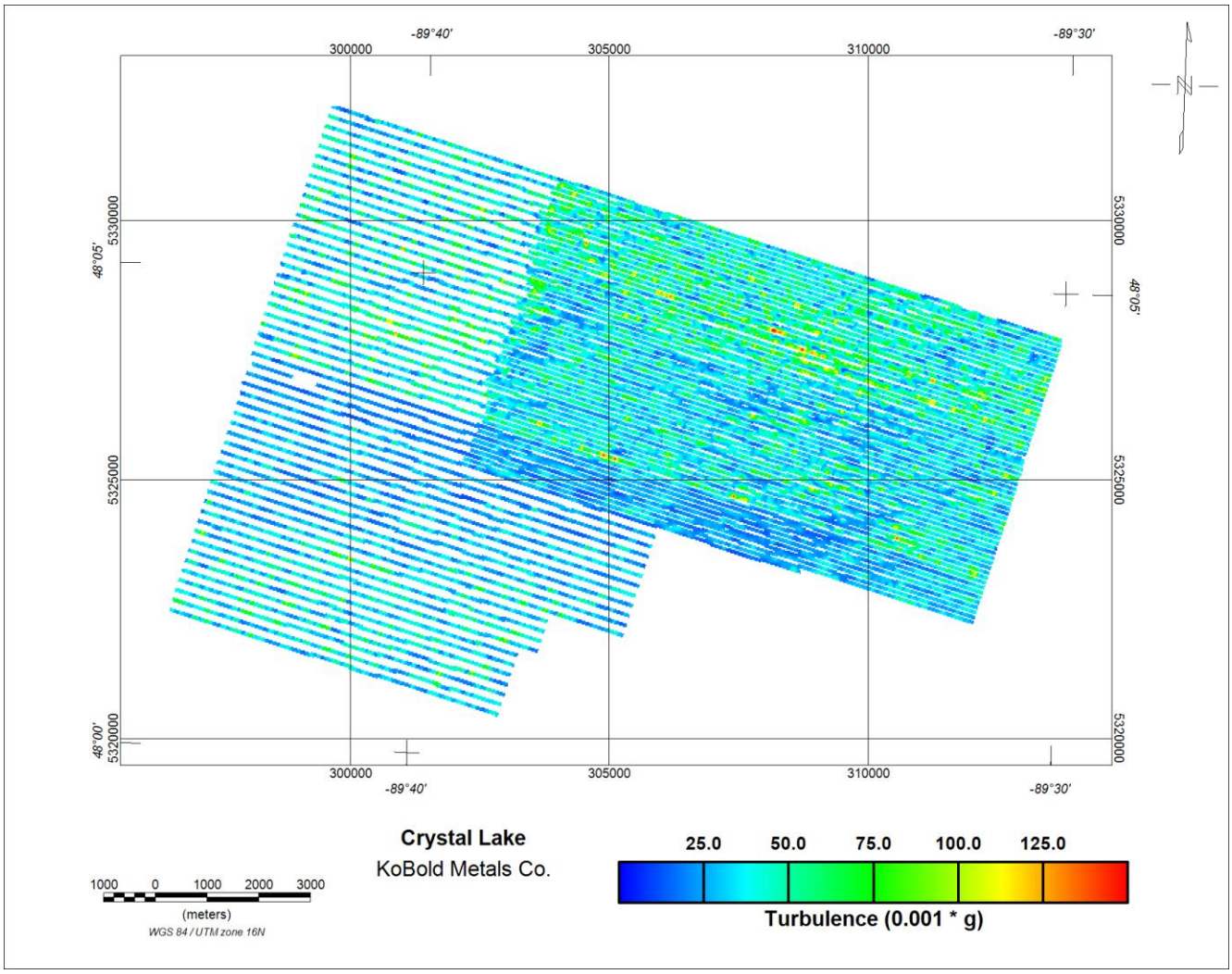

Figure 3: Crystal Lake – Turbulence (milli g where g = 9.80665 m/sec/sec)

4.4 AGG System Noise

The system noise is defined to be the standard deviation of half the difference between the A & B complements, for each of the NE and UV curvature components. The results for this survey were very good with values of 2.5 E for both the NE and UV components.

Figure 4 and *Figure 5* provide a representation of the variation in this standard deviation for each component. This is achieved by gridding a rolling measurement of standard deviation along each line using a window length of 100 data points.

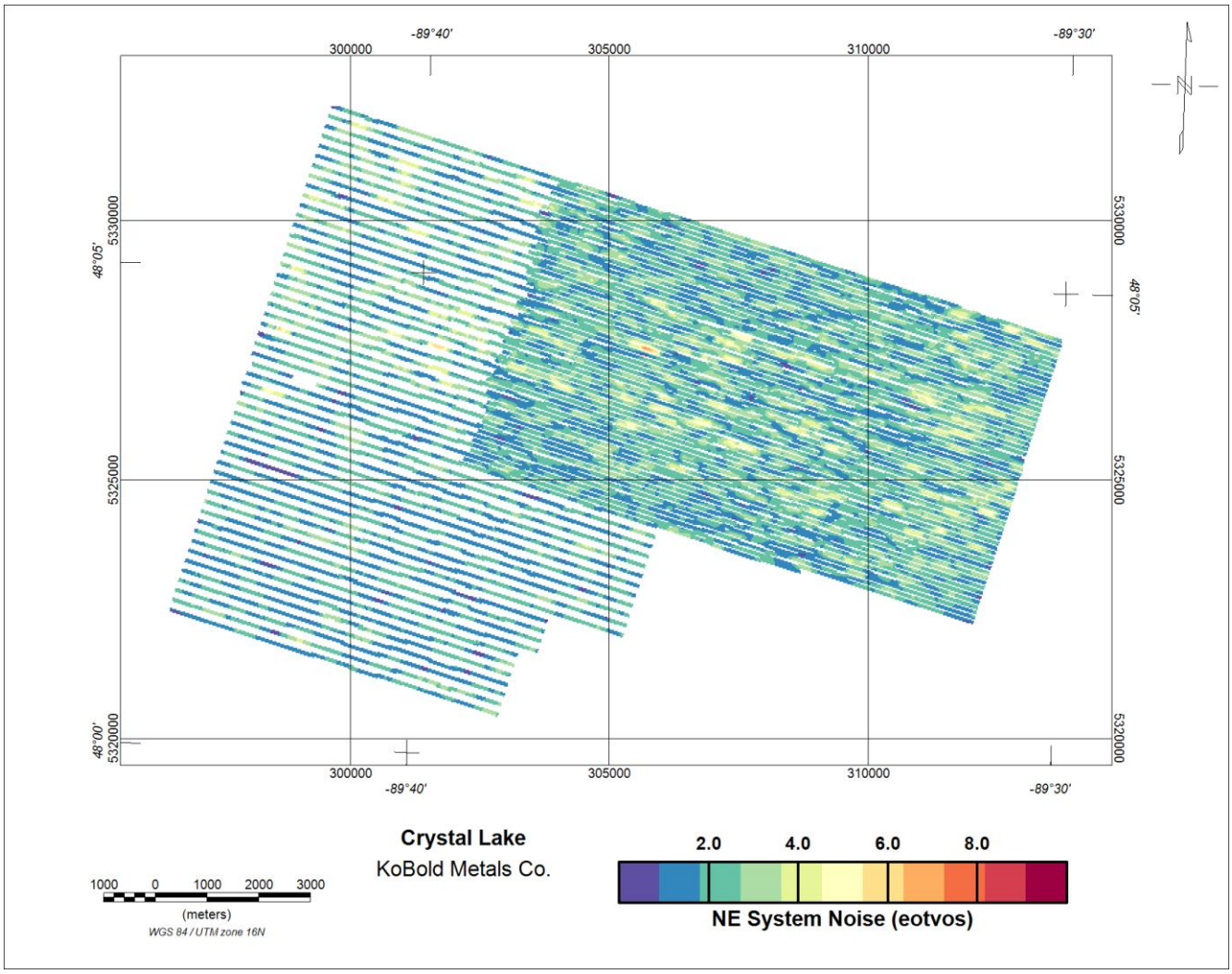

Figure 4: Crystal Lake – System Noise NE (eotvos)

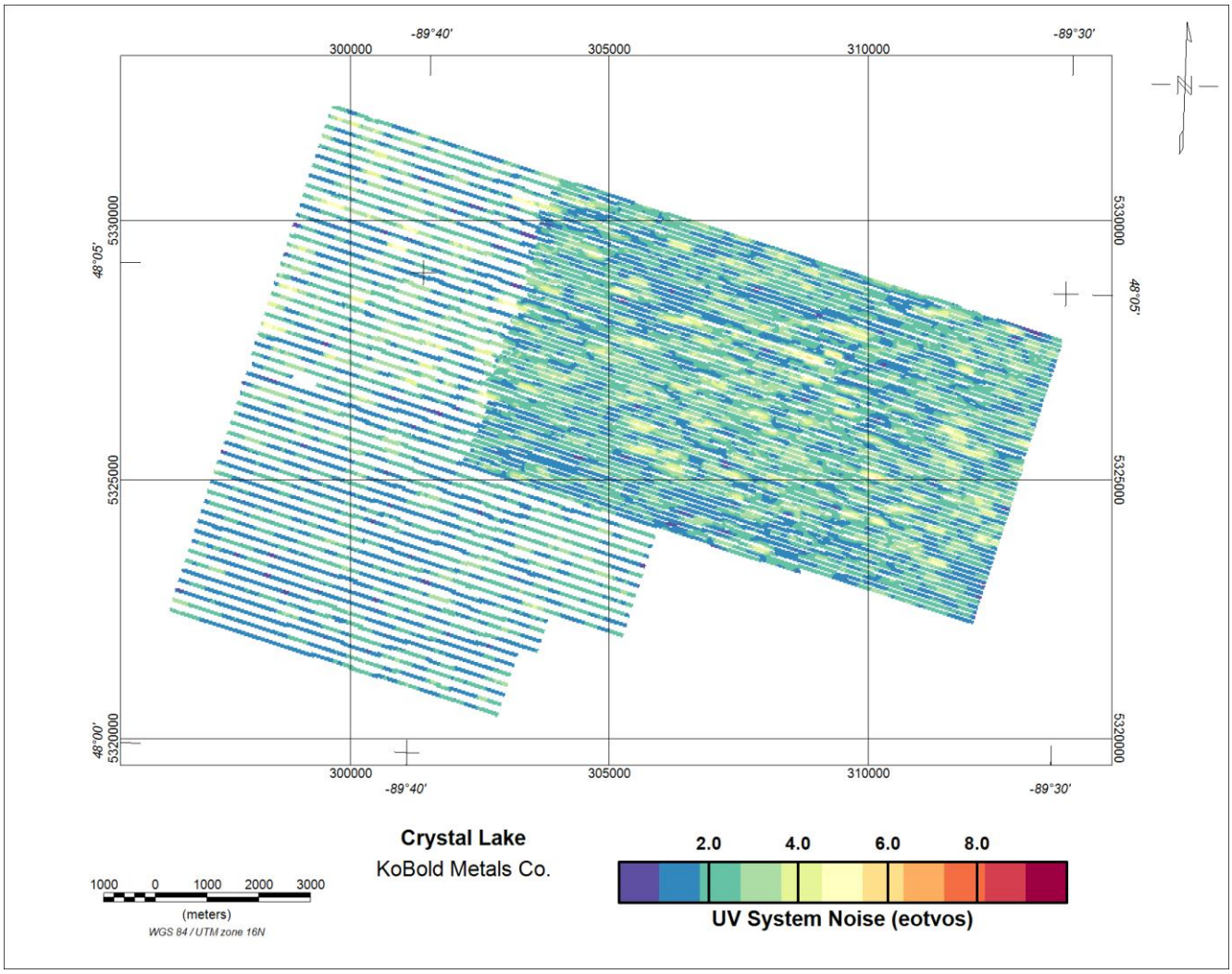

Figure 5: Crystal Lake – System Noise UV (eotvos)

4.5 Digital Terrain Model

Laser scanner range data were combined with GPS position and height data (adjusted from height above the WGS84 ellipsoid to height above the geoid by applying the Earth Gravitational Model 1996 (EGM96)). The output of this process is a “swath” of terrain elevations extending either side of the helicopter flight path. Width and sample density of this swath varies with helicopter height. Typical values are 100 to 150 metres and 5 to 10 metres respectively.

Because terrain correction of AGG data requires knowledge of the terrain at distances up to at least 40 km from the data location, laser scanner data collected only along the survey line path must be supplemented by data from another source.

For this purpose, Shuttle Radar Topography Mission (SRTM) v3 (one arc second resolution) data are used.

Laser scanner data quality was good with scan density generally above 90%. Laser scanner data were gridded at 10m with a 1 cell maximum extension beyond data limits. To fill gaps between lines and extend data coverage beyond the survey area, SRTM grid data were excised to an area 40 km beyond the planned survey area. The excised data were adjusted to the level of the laser scanner data using a grid difference adjustment method. The two grids were then combined into a single grid such that unmodified laser scanner data were used where defined and adjusted SRTM data were used to fill the gaps and extend the area.

Figure 6 shows the final Digital Terrain Model for the survey area.

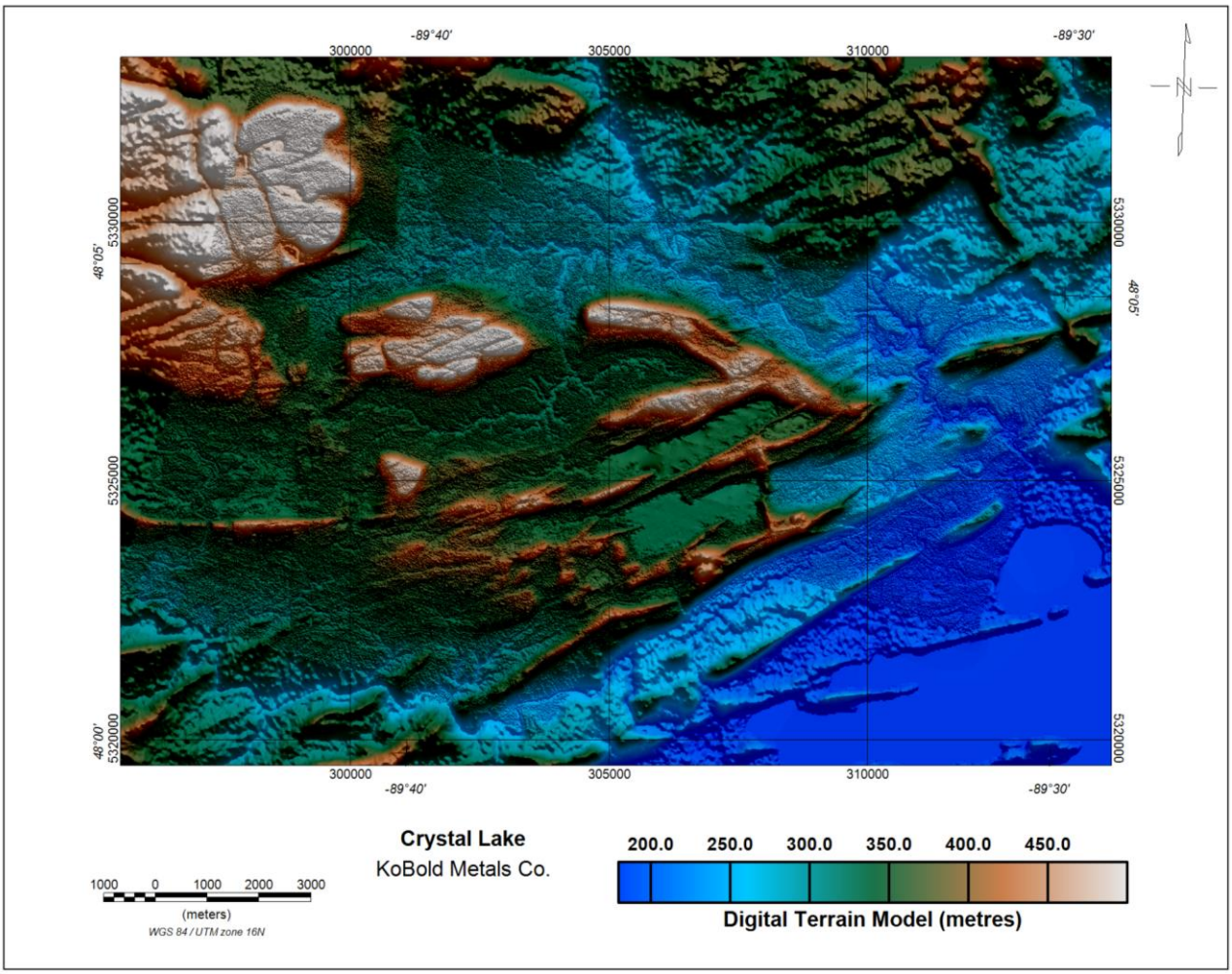

Figure 6: Crystal Lake – Final Digital Terrain Model (metres, referenced to the EGM96 geoid)

4.6 Terrain Clearance [Drape Surface Deviation]

Terrain clearance for the Crystal survey averaged slightly above the nominal clearance of 35 m having a mean value of 48.1 m across the survey area. The terrain clearance, as derived from laser scanner data, is shown in *Figure 7*.

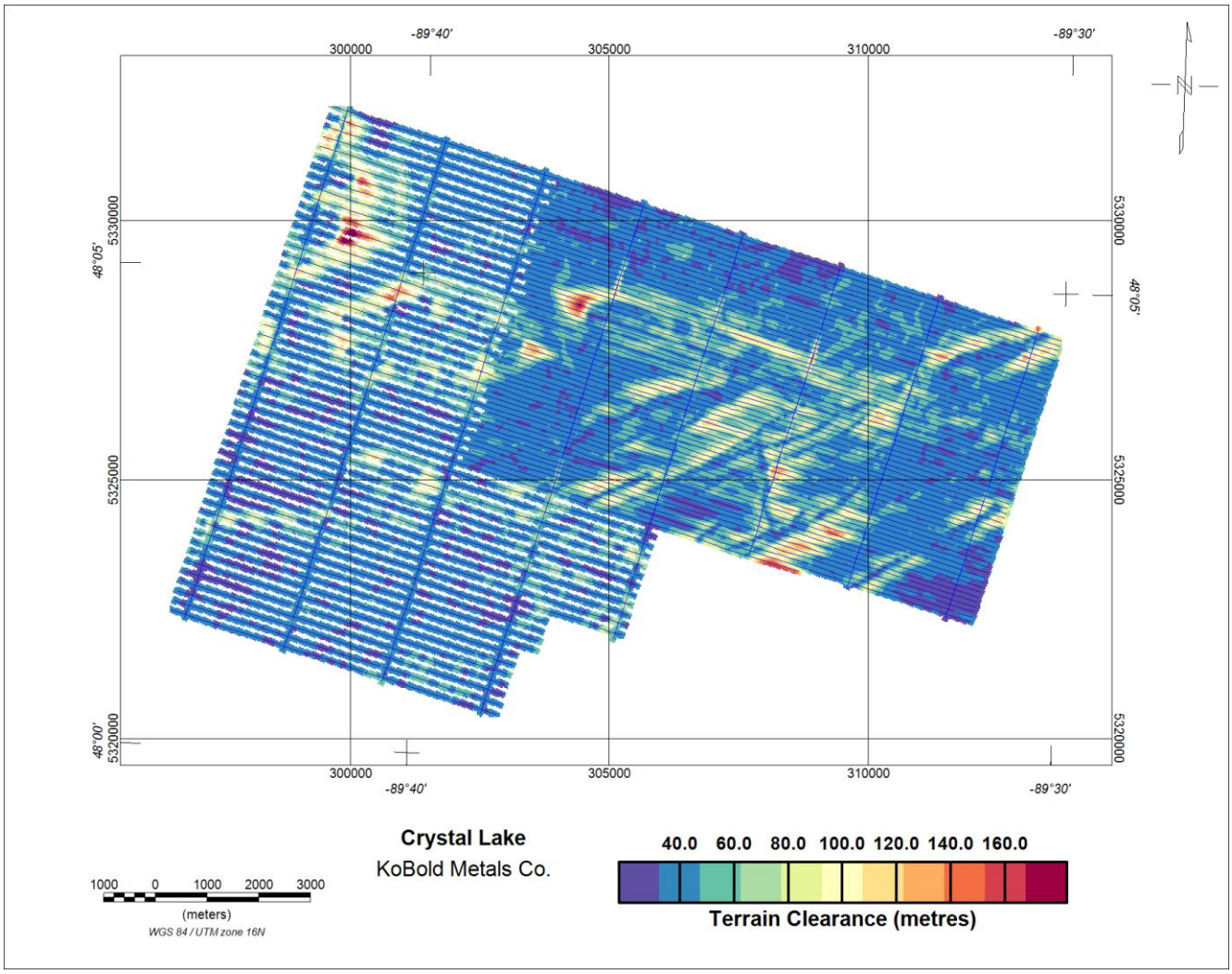

Figure 7: Crystal Lake – Terrain clearance derived from laser scanner data (metres)

5 HeliFALCON™ AIRBORNE GRAVITY GRADIENT (AGG) RESULTS

5.1 Processing Summary

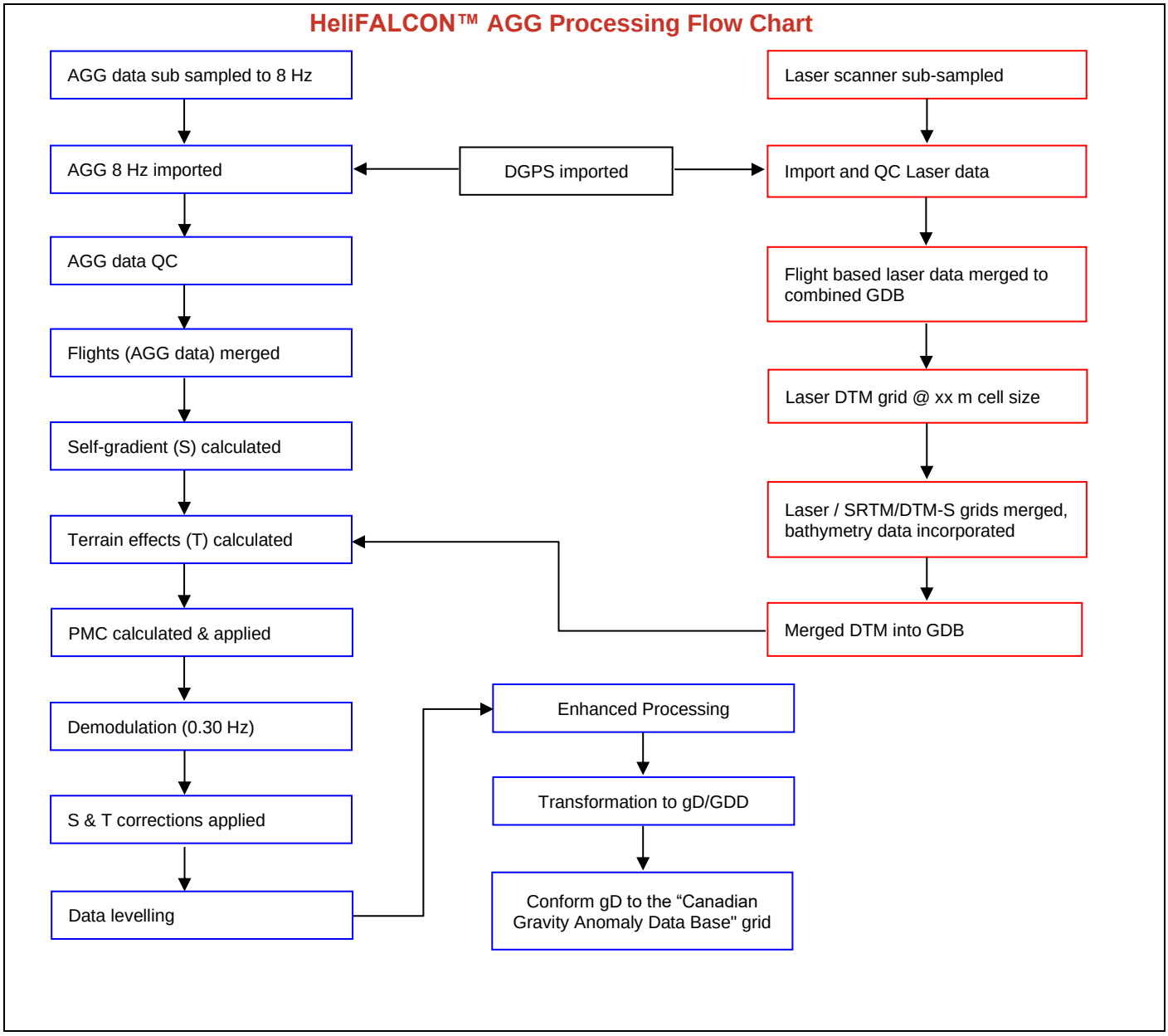

Figure 8: HeliFALCON™ AGG Data Processing

5.2 HeliFALCON™ Airborne Gravity Gradiometer Data

Figure 8 summarises the steps involved in processing the AGG data obtained from the survey.

The **HeliFALCON™** Airborne Gravity Gradiometer data were digitally recorded by the ADAS on removable hard drives. The raw data were then copied to the field processing laptop, backed up twice onto hard disk media and transferred by Secure File Transfer to the Xcalibur Multiphysics Jandakot data processing centre.

Preliminary processing and QC of the **HeliFALCON™** AGG data were completed on-site and at the Jandakot data processing centre using Xcalibur Multiphysics' AGG QC software. Further QC and final **HeliFALCON™** AGG data processing were performed at the Jandakot data processing centre.

5.3 Radar Altimeter Data

The terrain clearance measured by the radar altimeter in metres was recorded at 10 Hz. The data were plotted and inspected for quality.

5.4 Laser Scanner Data

Laser scanner returns were recorded at a rate of 36 scans per second with each scan returning 276 data points. Each return was converted to ground surface elevation by combining scanner range and angle data with helicopter position and attitude data. Computed elevations were then sub sampled by first dividing each scan into ten segments and combining five adjacent scans per segment, then using a special algorithm to select the optimum return within each data "bin" thus formed. Sub-sampled laser scanner data were edited to remove spikes prior to gridding.

5.5 Positional Data

Differential GPS processing was applied to compute accurate helicopter positions once per second. Waypoint's GrafNav GPS processing software calculated DGPS positions using raw range data obtained from receivers in the helicopter and at a fixed ground base station.

The GPS ground station position was determined by sending several hours of collected data to an online GPS processing service to obtain a differentially corrected computed position. The service selected was AUSPOS, which is provided by Geoscience Australia. The GPS data were processed and quality controlled using the WGS84 datum.

Parameters for the WGS84 datum are:

Ellipsoid: WGS84

Semi-major axis: 6,378,137.0 m

Inverse flattening (1/f): 298.257

All processing was performed using WGS84/UTM Zone 16N coordinates. Final line data and final grid data were supplied in this projection.

5.6 Terrain Correction

Terrain corrections were derived from the digital terrain model grid for every data point in the survey. A terrain density of 1.00 g/cm^3 was used to compute the terrain correction channels, which were then multiplied by the chosen correction density before being subtracted from the data.

In consultation with the Client, a correction density of 2.2 g/cm^3 was selected as approximating most closely the density of the terrain in the survey area and was applied. As standard, a density of 2.67 g/cm^3 was also applied and these data are also included.

5.7 Tie line Levelling

The terrain corrected data and the uncorrected data were then tie line levelled separately for each block.

5.8 Enhanced Processing

The enhanced processing technique improves the noise amplitude density (as discussed by Christensen et al, 2015) by 25-50% for surveys with line spacing of less than 1 km. The method exploits the different spatial frequencies of system noise and geologic signal. After converting the data into the 2D spatial domain, a custom spatial filter is applied that removes the system noise, while retaining the remaining geologic signal. The process will limit the data resolution to the survey line spacing.

5.9 HeliFALCON™ Airborne Gravity Gradient Data - G_{DD} & g_D

The transformation into G_{DD} and g_D was accomplished using a Fourier domain transformation method.

5.9.1 Fourier

The Fourier domain transformation method firstly calculates many flat surfaces at constant intervals between the lowest and highest-flying altitude. The transformation is performed on each of these surfaces and the result is a three-dimensional array for each tensor component where each level corresponds to a flat layer of a constant flying height. Using an approximation, the data is interpolated from this array back onto the processing drape surface.

5.9.2 Drape Surfaces

The transformation uses a smoothed surface onto which the output data are projected. This surface is a smoother equivalent of the actual flying surface.

The Fourier (density 2.2 g/cm^3) G_{DD} map is shown in *Figure 9*.

The Fourier vertical gravity (g_D), derived by integrating $G_{DD,}$ (density 2.2 g/cm^3) result is presented in *Figure 10*.

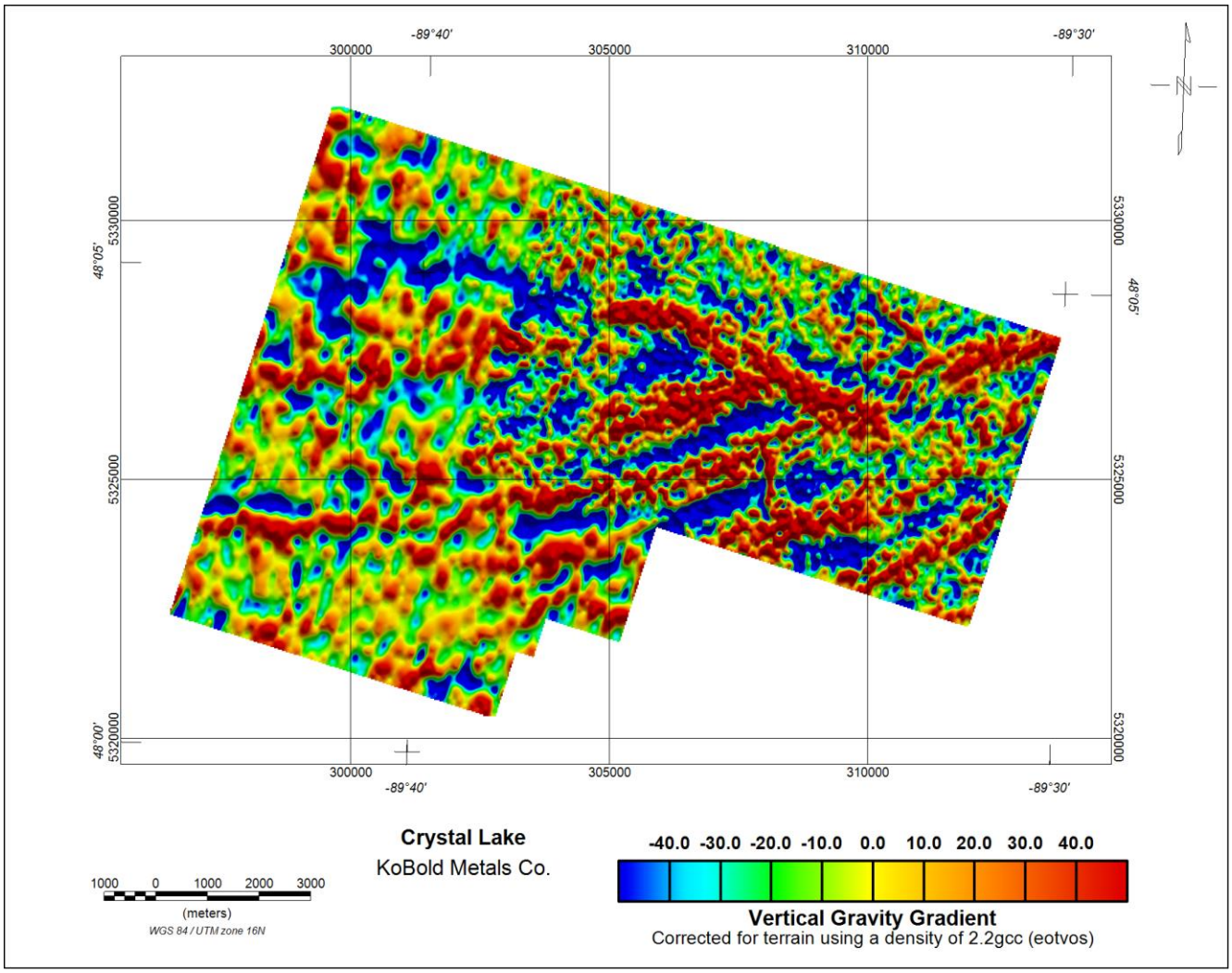

Figure 9: Crystal Lake – Enhanced Vertical Gravity Gradient (GDD)

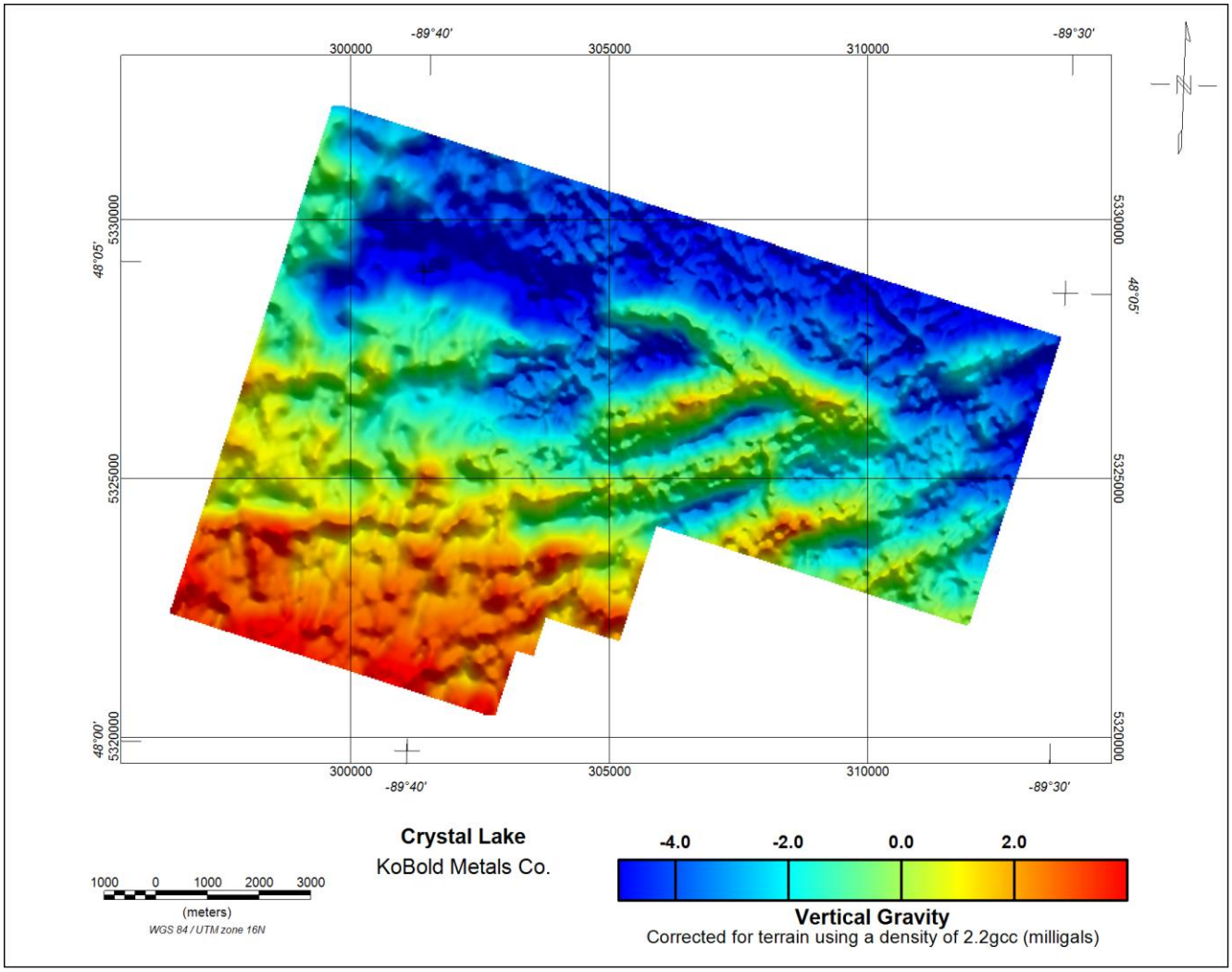

Figure 10: Crystal Lake – Enhanced Vertical Gravity (gD)

5.10 Conforming gD to regional gravity

As discussed in section *8.3,* the long wavelength information in g_D can be improved by incorporating ancillary information. Such information is available in the form of the Canadian Gravity Anomaly Data Base.

The Fourier and equivalent source g_D and G_{DD} grids were conformed to grids derived from a subset of the Canadian Gravity Anomaly Data Base and gravity data provided by the client as follows. The g_D (density 2.2 g/cm^3) results are presented in *Figure 11*.

- Low pass filter the regional data using a cosine squared filter with cut-off at 7 km, tapering to 5 km.
- High pass filter the g_D data (Fourier and equivalent source) using a cosine squared filter with cut-off at 7 km, tapering to 5 km.
- Conform the data to the regional data by addition of the filtered grids. The filter design is such that this method provides uniform frequency response across the overlap frequencies.

Further discussion of this method can be found in Dransfield (2010).

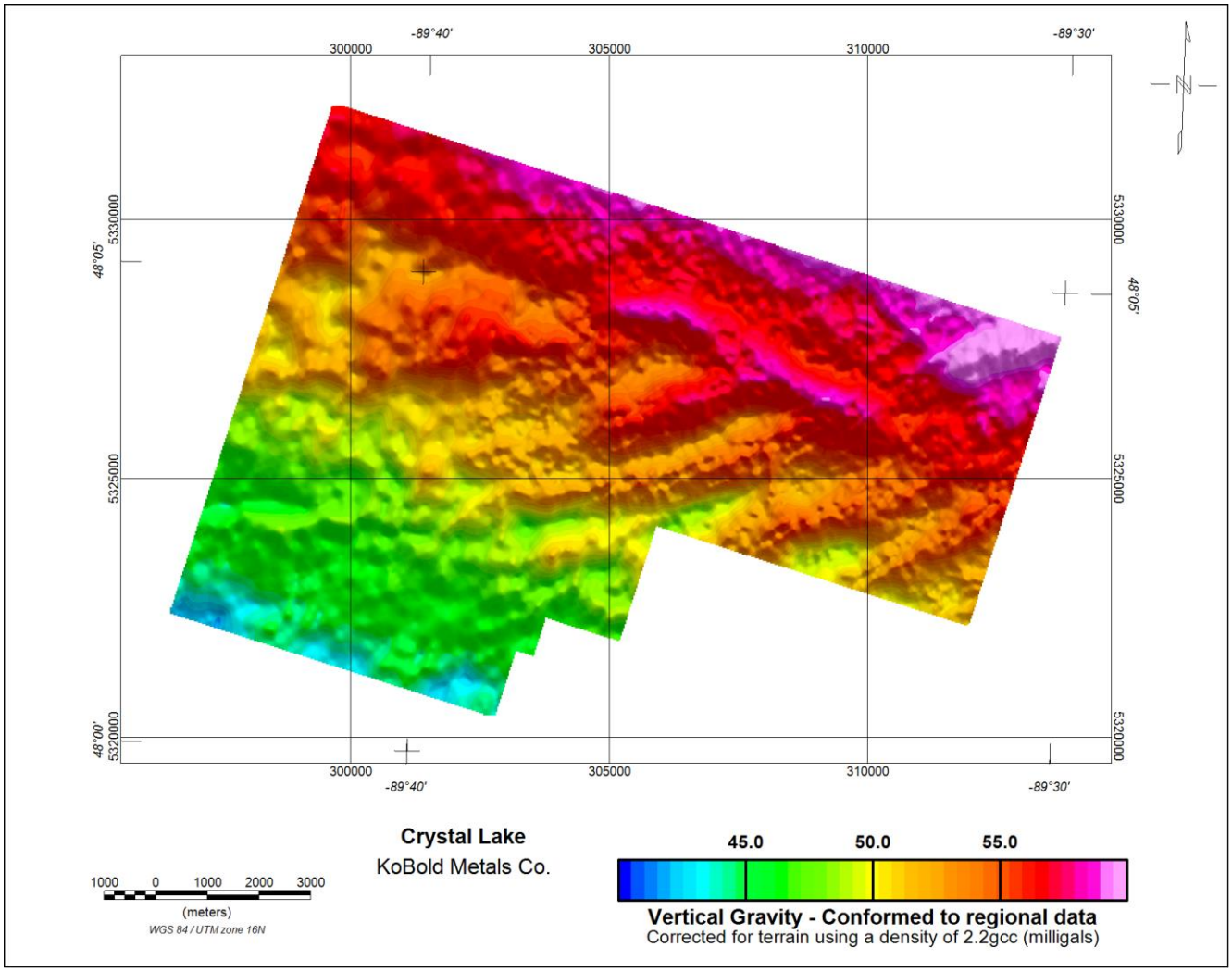

Figure 11: Crystal Lake – Enhanced Vertical Gravity (gD) conformed to regional gravity data

5.11 Processing Summary

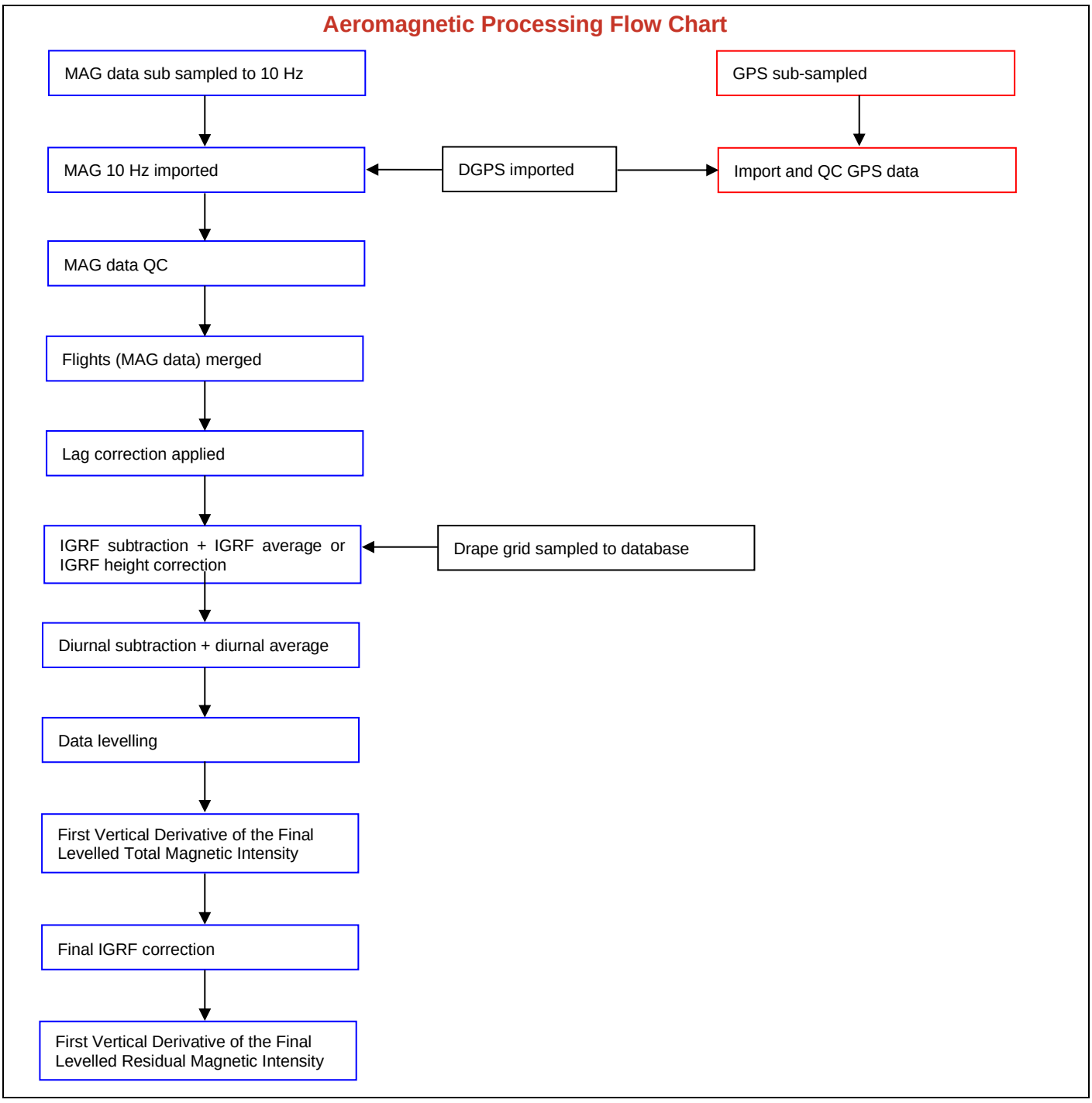

Figure 12: Aeromagnetic Data Processing

5.12 Aeromagnetic Data

Figure 12 summarises the steps involved in processing the aeromagnetic data obtained from the survey.

The aeromagnetic data were digitally recorded by the FASDAS on removable hard drives. The raw data were then copied onto the field processing laptop, backed up twice onto hard drive media and sent via FTP to Xcalibur Multiphysics' secure server.

Preliminary QC of the aeromagnetic data was completed on-site using Xcalibur Multiphysics' proprietary ATLAS software. Further QC and aeromagnetic data processing were performed by the office-based data processor.

5.13 Radar Altimeter Data

Refer to section *5.3* for radar altimeter data.

5.14 Positional Data

Refer to section *5.5* for positional data processing.

5.15 Lag Correction

All aeromagnetic data were lagged prior to final processing. A lag of 0.4 seconds was applied.

5.16 IGRF Correction

The IGRF model 2020 was calculated at date 29th March, 2020, using the GPS height for each magnetic reading. This value was subtracted from each magnetic reading to produce an IGRF corrected residual magnetic intensity.

5.17 Diurnal Subtraction

The edited base station magnetics (diurnal) were filtered using a long wavelength filter to retain wavelengths longer than xx seconds. This value was subtracted from the IGRF corrected total magnetic intensity. Next, based upon the average magnetic value calculated from running the base station for 24 hours, a base value of 55700 nT was added back to the magnetics. This produced the diurnally corrected total magnetic intensity.

5.18 Tie line Levelling

The IGRF and diurnally corrected total magnetic intensity data were tie line levelled using Xcalibur Multiphysics' proprietary ATLAS software.

5.19 Line Levelling

The IGRF and diurnally corrected total magnetic intensity data were then passed through a proprietary line levelling adjustment process, optimised for the survey.

5.20 Micro-levelling

The total magnetic intensity data were micro-levelled using Xcalibur Multiphysics' proprietary ATLAS software.

5.21 Final Magnetic Intensity

The final magnetic intensity is presented in *Figure 13*.

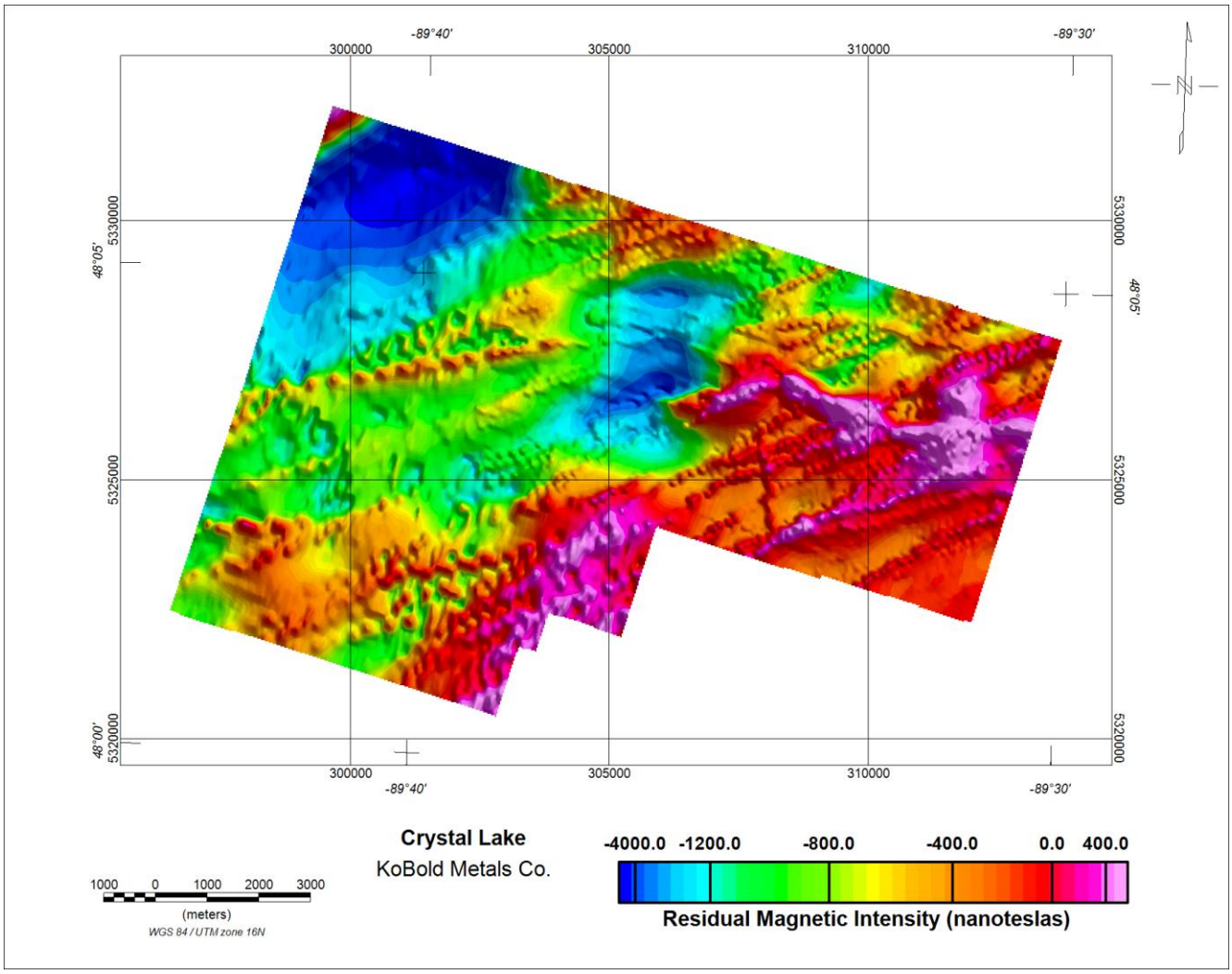

Figure 13: Crystal Lake – Final Magnetic Intensity (nT)

5.22 First Vertical Derivative of the Final Magnetic Intensity

The first vertical derivative of the final magnetic intensity is presented in *Figure 14*.

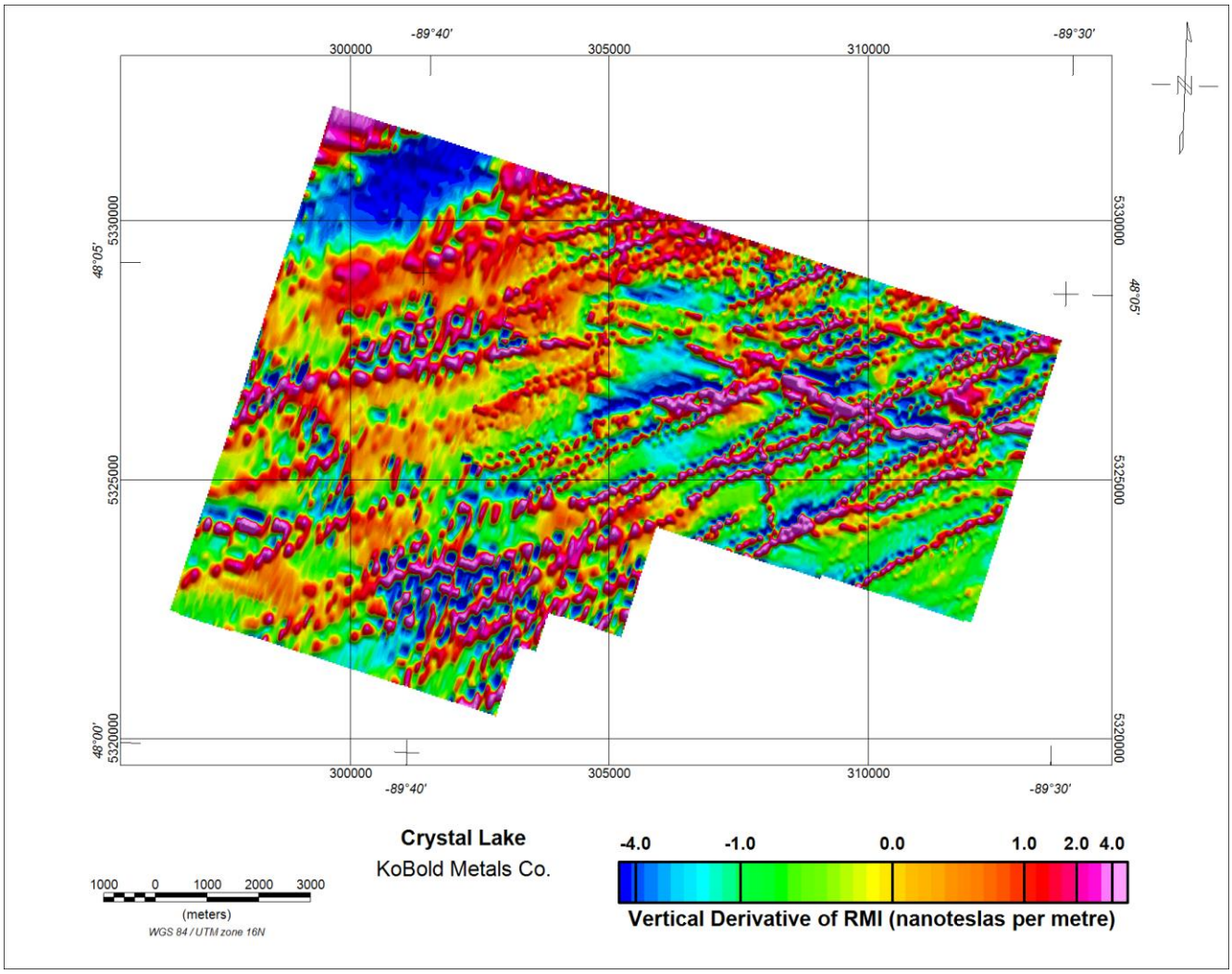

Figure 14: Crystal Lake – First Vertical Derivative of the Final Magnetic Intensity (nT/m)

6 APPENDIX I - SURVEY EQUIPMENT

6.1 Survey Helicopter

A Helicarrier Inc Eurocopter AS350-B3, Canadian registration C-FHCH, was used to fly the survey area. The following instrumentation was used for this survey.

6.2 HeliFALCON™ Airborne Gravity Gradiometer

HeliFALCON™ AGG System (Kepler)

The **HeliFALCON™** AGG System is based on current state-of-the-art airborne gravity gradiometer technology and has been optimized for airborne broadband geophysical exploration. The system is capable of supporting surveying activities in areas ranging from 1,000 ft below sea level to 13,000 ft above sea level with helicopter speeds from 30 to 130 knots. The HeliFALCON™ AGG data streams were digitally recorded at different rates on removable drives installed in the HeliFALCON™ AGG electronics rack.

6.3 Airborne Data Acquisition Systems

Digital Acquisition System (HeliDAS)

The HeliDAS is a data acquisition system executing propriety software for the acquisition and recording of location, magnetic and ancillary data. Data are presented both numerically and graphically in real time on the VGA display providing on-line quality control capability.

The HeliDAS is also used for real time navigation. A pre-programmed flight plan containing boundary coordinates, line start and end coordinates, altitude values calculated for a theoretical drape surface, line spacing and cross track definitions is loaded into the computer prior to each flight. The WGS84 latitude, longitude and altitude received from the real-time corrected, dual frequency Novatel positioning receiver, is transformed to the local coordinate system for cross track and distance to go values. This information, together with ground heading and speed, is displayed to the pilot numerically and graphically on a two-line LCD display. It is also presented on the operator LCD screen in conjunction with a pictorial representation of the survey area, survey lines and ongoing flight path.

HeliFALCON™ AGG Data Acquisition System (ADAS)

The ADAS provides control and data display for the HeliFALCON™ AGG system. Data are displayed in real time for the operator and warnings displayed should system parameters deviate from tolerance specifications. All HeliFALCON™ AGG and laser scanner data are recorded to a removable hard drive.

6.4 Aerial and Ground Magnetometers

The airborne Caesium magnetometer was a **Scintrex CS-3** having a noise envelope of 0.05 nT pk-pk, 0.1 Hz bandwidth.

The ground magnetometer was a **Scintrex CS-3** Caesium sensor sampling at 1 Hz.

6.5 Real-Time Differential GPS

The **Novatel OEMV-3G** multi-frequency positioning receiver provides real-time differential GNSS for the on-board navigation system. The OEMV-3 is designed to track the GPS L1 and L2 signals, as well as GLONASS L1 and L2. The differential data set is relayed via a geo-synchronous satellite to the aircraft where the receiver optimized the corrections for the current location.

6.6 GPS Base Station Receiver

The **Novatel OEM4** is a multi-channel, L1/L2 GNSS receiver. It provides raw range information of all satellites in view sampled every second and recorded on a computer laptop. These data are used to provide post-processed differential GNSS (DGNSS) corrections for the rover data flight path.

6.7 Altimeters

Sperry RT-300 Radar Altimeter

The radar altimeter has a sensitivity of 1 ft, a range of 0-2,500 ft and a measurement rate of 10 Hz.

6.8 Laser Scanner

Riegl VUX-1UAV

The laser scanner is designed for high-speed line scanning applications in conjunction with an external IMU unit. The system is based upon the principle of time-of-flight measurement of short laser pulses in the near infrared wavelength region and the angular deflection of the laser beam is obtained by a rotating polygon mirror wheel. At a laser pulse repetition rate of 51.48 kHz, the measurement range is up to 1050 m (depending on reflectivity) with a minimum range of 3 m and an accuracy of 10 mm (1 sigma @ 150 m range under Riegl test conditions). The laser beam is eye-safe, the laser wavelength is near infrared, the scan angle range is up to ± 80º and the scan speed is up to 200 scans/s.

6.9 Data Processing Hardware and Software

The following equipment and software were used:

Hardware

- One 2.0 GHz (or higher) laptop computer
- External USB hard drive reader for ADAS removable drives
- Two External USB hard drives for data backup
- All-In-One printer, copier, scanner

Software

- Oasis Montaj data processing and imaging software
- GrafNav Differential GPS processing software
- Xcalibur Multiphysics' Atlas data processing software
- Xcalibur Multiphysics' DiAGG processing software

7 APPENDIX II - SYSTEM TESTS

7.1 Instrumentation Lag

Due to the relative position of the magnetometer, altimeters and GPS antenna on the helicopter and to processing/recording time lags, raw readings from each data stream vary in position. To correct for this and to align selected anomaly features on lines flown in opposite directions, the magnetic and altimeter data are 'parallaxed' with respect to the position information. The lags were applied to the data during processing.

7.2 Radar Altimeter Calibration

The radar altimeter is checked for accuracy and linearity every 12 months, or when any change in a key system component requires this procedure to be carried out. This calibration allows the radar altimeter data to be compared and assessed with the other height data (GPS, barometric and laser) to confirm the accuracy of the radar altimeter over its operating range. The calibration is performed by flying a number of 30-second lines at preselected terrain clearances over an area of flat terrain and using the results of the radar altimeter, differentially corrected GPS heights in mean sea level (MSL) and laser scanner were used to derive slope and offset information.

7.3 Magnetometer Compensation

The magnetometer compensation corrects the magnetometer readings for the effect of the magnetic field of the aircraft, both static and dynamic, on the readings.

The compensation correction is calculated using a fluxgate magnetometer to measure the aircraft's manoeuvres. Manoeuvres consist of ±5 degree rolls, ±10 degree pitches and ±5 degree yaws peak to peak over periods of 5 seconds repeated in each line direction. The magnetometer compensation is repeated when a change big enough to impact on the magnetometer has been made to the aircraft or its contents. A magnetometer compensation is normally performed in an area with similar magnetic declination, inclination and field strength to the survey area, i.e. close to or within the survey area.

7.4 HeliFALCON™ AGG Noise Measurement

At the commencement of the survey, 20 minutes of data were collected with the helicopter in straight level flight at 3500 ft AGL. These data were assessed in-flight to check the AGG noise levels.

Daily flight debriefs incorporating **HeliFALCON™** AGG performance statistics for each flight line are prepared using output from Xcalibur Multiphysics' DiAGG software. These are sent daily to Xcalibur Multiphysics' office staff for performance evaluation.

7.5 Daily Calibrations

A set of daily calibrations were performed each survey day as follows:

- Magnetic base station time check
- AGG Quiescent Calibration

7.5.1 Magnetic Base Station Time Check

Prior to each day's survey, all magnetic base stations were synchronised using broadcast GPS time signals.

7.5.2 HeliFALCON™ AGG Calibration

A calibration was performed at the beginning of each flight and the results monitored by the operator. The coefficients obtained from each of the calibrations were used in the processing of the data.

8 APPENDIX III - HeliFALCON™ AGG DATA & PROCESSING

8.1 Nomenclature

The **HeliFALCON™** airborne gravity gradiometer (AGG) system adopts a North, East, and Down coordinate sign convention and these directions (N, E, and D) are used as subscripts to identify the gravity gradient tensor components (gravity vector derivatives). Lower case is used to identify the components of the gravity field and upper case to identify the gravity gradient tensor components. Thus, the parameter usually measured in a normal exploration ground gravity survey is $\mathbf{g_D}$ and the vertical gradient of this component is $\mathbf{G_{DD}}$.

8.2 Units

The vertical component of gravity ($\mathbf{g_D}$) is delivered in the usual units of mGal. The gradient tensor components are delivered in eotvos, which is usually abbreviated to "E". By definition **1 E = 10^{-4} mGal/m.**

8.3 HeliFALCON™ Airborne Gravity Gradiometer Surveys

In standard ground gravity surveys, the component measured is "$\mathbf{g_D}$", which is the *vertical component of the acceleration due to gravity*. In airborne gravity systems, since the aircraft is itself accelerating, measurement of "$\mathbf{g_D}$" cannot be made to the same precision and accuracy as on the ground. Airborne gravity gradiometry uses a differential measurement to remove the aircraft motion effects and delivers gravity data of a spatial resolution and sensitivity comparable with ground gravity data.

The **HeliFALCON™** gradiometer instrument acquires two curvature components of the gravity gradient tensor namely $\mathbf{G_{NE}}$ and $\mathbf{G_{UV}}$ where $\mathbf{G_{UV}} = (\mathbf{G_{NN}} - \mathbf{G_{EE}})/2$.

A feature of the **HeliFALCON™** AGG system is that two independent measurements are made of both the NE and UV curvature components. This is achieved by using two sets of accelerometers, referred to as the A complement and the B complement. Each complement consists of four accelerometers. The measured gradients from these complements are referred to as A_{NE} and A_{UV} and B_{NE} and B_{UV}. The $\mathbf{G_{NE}}$ and $\mathbf{G_{UV}}$ gradients are computed by averaging A and B:

$$G_{NE} = \frac{(A_{NE} + B_{NE})}{2}$$

$$G_{UV} = \frac{(A_{UV} + B_{UV})}{2}$$

Since these curvature components cannot easily and intuitively be related to the causative geology, they are transformed into the vertical gravity gradient ($\mathbf{G_{DD}}$), and integrated to derive the vertical component of gravity ($\mathbf{g_D}$). Interpreters display, interpret and model both $\mathbf{G_{DD}}$ and $\mathbf{g_D}$. The directly measured $\mathbf{G_{NE}}$ and $\mathbf{G_{UV}}$ data are appropriate for use in inversion software to generate density models of the earth. The vertical gravity gradient, $\mathbf{G_{DD}}$, is more sensitive to small or shallow sources and has greater spatial resolution than $\mathbf{g_D}$ (similar to the way that the vertical magnetic gradient provides greater spatial resolution and increased sensitivity to shallow sources of the magnetic field). In the integration of $\mathbf{G_{DD}}$ to give $\mathbf{g_D}$, the very long wavelength component, at wavelengths comparable to or greater than the size of the survey area, cannot be fully recovered. Long wavelength gravity data are therefore incorporated in the $\mathbf{g_D}$ data from other sources. This might be regional ground, airborne or marine gravity if such data are available. The Danish Technical University global gravity data of 2013 (DTU13) are used as a default if other data are not available.

8.4 Gravity Data Processing

The main elements and sequence of processing of the gravity data are given below. Unless not applicable or specified otherwise, the processing step is applied to each individual complement element (A_{NE}, A_{UV}, B_{NE}, B_{UV}):

1. Dynamic corrections for residual aircraft motion (called Post Mission Compensation or PMC) are calculated and applied.
2. Self-gradient corrections are calculated and applied to reduce the time-varying gradient response from the aircraft and platform.
3. A Digital Terrain Model (DTM) is created from the laser scanner range data, the AGG inertial navigation system rotation data and the DGPS position data.
4. Terrain corrections are calculated and applied.
5. Line levelling and micro-levelling (where necessary) are applied.
6. $\mathbf{G_{NE}}$ and $\mathbf{G_{UV}}$ are transformed into the full gravity gradient tensor, including $\mathbf{G_{DD}}$, and into $\mathbf{g_D}$.

8.5 Aircraft Dynamic Corrections

The design and operation of the **HeliFALCON™** AGG results in very considerable reduction of the effects of aircraft acceleration but residual levels are still significant and further reduction is required and must be done in post-processing.

Post-processing correction relies on monitoring the inertial acceleration environment of the gravity gradiometer instrument (GGI) and constructing a model of the response of the GGI to this environment. Parameters of the model are adjusted by regression to match the sensitivity of the GGI during data acquisition. The modelled GGI output in response to the inertial sensitivities is subtracted from the observed output. Application of this technique to the output of the GGI, when it is adequately compensated by its internal mechanisms, reduces the effect of aircraft motion to acceptable levels.

Following these corrections, the gradient data are demodulated and filtered along line using a 6-pole Butterworth low-pass filter with a cut-off frequency of 0.30 Hz.

8.6 Self-gradient Corrections

The GGI is mounted in gimbals controlled by an inertial navigation system, which keeps the GGI pointing in a fixed direction whilst the aircraft and gimbals rotate around it. Consequently, the GGI measures a time-varying gravity gradient due to these masses moving around it as the heading and attitude of the aircraft changes during flight. This is called the self-gradient.

Like the aircraft dynamic corrections, the self-gradient is calculated by regression of model parameters against measured data. In this case, the rotations of the gimbals are the input variables of the model. Once calculated, the modelled output is subtracted from the observed output.

8.7 Laser Scanner Processing

The laser scanner measures the range from the aircraft to the ground in a swath of angular width ±40/80 degrees below the aircraft. The aircraft attitude (roll, pitch and heading) data provided by the [AGG inertial navigation system][on-board IMU] are used to adjust the range data for changes in attitude and the processed differential GPS data are used to reference the range data to located ground elevations referenced to the WGS84 datum (corrected for the EGM96 geoid separation model). Statistical filtering strategies are used to remove anomalous elevations due to foliage or built-up environment. The resulting elevations are gridded to form a digital terrain model (DTM).

8.8 Terrain Corrections

An observation point above a hill has excess mass beneath it compared to an observation point above a valley. Since gravity is directly proportional to the product of the masses, uncorrected gravity data have a high correlation with topography.

It is therefore necessary to apply a terrain correction to gravity survey data. For airborne gravity gradiometry at low survey heights, a detailed DTM is required. Typically, immediately below the aircraft, the digital terrain will need to be sampled at a cell size roughly one-third to one-half of the survey height and with a position accuracy of better than 1 metre. For these accuracies, LIDAR data are required and each **HeliFALCON™** survey aircraft comes equipped with LIDAR (laser scanner).

If bathymetric data are used, then these form a separate terrain model for which terrain corrections are calculated at a density chosen to suit the water bottom – water interface.

Once the DTM has been merged, the terrain corrections for each of the $\mathbf{G_{NE}}$ and $\mathbf{G_{UV}}$ data streams are calculated. In the calculation of terrain corrections, a density of 1 g/cm^3 is used. The calculated corrections are stored in the database allowing the use of any desired terrain correction density by subtracting the product of desired density and correction from the measured $\mathbf{G_{NE}}$ and $\mathbf{G_{UV}}$ data. The terrain correction density is chosen to be representative of the terrain density over the survey area. Sometimes more than one density is used with input from the Client.

Typically, the terrain corrections are calculated over a distance 40 to 60 km from each survey measurement point.

8.9 Tie line Levelling

The terrain and self-gradient corrected $\mathbf{G_{NE}}$ and $\mathbf{G_{UV}}$ data are tie line levelled across the entire survey using a least-squares minimisation of differences at survey line intersections. Occasionally some micro-levelling might be performed.

8.10 Regional Levelling

The terrain and self-gradient corrected $\mathbf{G_{NE}}$ and $\mathbf{G_{UV}}$ data are adjusted to the regional data, separately for each line. Occasionally some micro-levelling might be performed.

8.11 Transformation into GDD & g_D

The transformation of the measured, corrected and levelled $\mathbf{G_{NE}}$ and $\mathbf{G_{UV}}$ data into gravity and components of the full gravity gradient tensor is accomplished using two methods:

- Fourier domain transformation
- Equivalent source transformation

The input data for the Fourier method are the average **NE** and **UV** components computed from the complement data, as described in section *8.3*. The Fourier method relies on the Fourier transform of Laplace's equation. The application of this transform to the complex function $\mathbf{G_{NE} + i\ G_{UV}}$ provides a stable and accurate calculation of each of the full tensor components and gravity. The Fourier method performs piece-wise upward and downward continuation to work with data collected on a surface that varies from a flat horizontal plane. For stability of the downward continuation, the data are low-pass filtered. The cut-off wavelength of this filter depends on the variations in altitude range and line spacing. It is set to the smallest value that provides stable downward continuation.

In survey areas where the variability of the terrain surface (and hence the flight surface) makes it impossible to obtain Fourier transformation results that are both high resolution and stable, an alternate method can be applied which bypasses the upward and downward continuation steps. The results are calculated at the flight surface. This approach lacks the mathematical rigour of the complete method but allows for greater detail in the output data. It must be noted however that, if the terrain is too extreme, this method may fail to accurately transform the input data. This can be checked by comparing the input GNE and GUV data with the predicted values of the same data after transformation. If they do not match well, the Fourier transformation method cannot be relied upon.

The input data for the equivalent source method are the individual **NE** and **UV** component data from each complement, as referred to in section *8.3*. The equivalent source method relies on a smooth model inversion to calculate the density of a surface of sources and from these sources; a forward calculation provides the $\mathbf{G_{DD}}$ and $\mathbf{g_D}$ data as well as the other gradient tensor components. The effect of the smoothing is similar to but not the same as the application of the low-pass filter in the Fourier domain method. In areas of highly variable terrain, flying low can lead to some instability in the equivalent source method as the computation surface approaches the location of the derived sources. It may be necessary to accept some localised instability in order to optimise the overall result.

The equivalent source procedure defines an array of rectangular (usually square) plates, extending slightly past the survey area in all directions. Each plate is assumed to have uniform (but initially unknown) surface density and to lie on a predefined solution surface. Using the individual NE and UV component data measured at the centre of each plate, a system of linear equations is formed which can then be solved for the density of each plate using a least squares inversion method. Once the plate density distribution is determined, it can be used for forward calculation of all tensor components and of vertical gravity.

The limitations of gravity gradiometry in reconstructing the long wavelengths of gravity can lead to differences in the results of these two methods at long wavelength. The merging of the $\mathbf{g_D}$ data with externally supplied regional gravity such as the DTU13 gravity provides a way of reducing these differences. The application of this procedure will depend on the survey size and resolution of available regional gravity. If survey size is too small or regional gravity resolution too large, regional conforming is not applied.

8.12 Terrain Corrections Using Alternate Terrain Densities

Although both uncorrected processed and transformed data and unit density terrain correction data are supplied, it is not recommended that these be used to create final data corrected for any arbitrary terrain correction density. The principal reason for this is that tie line levelling occurs after application of the terrain correction. As a result, levelling errors present in the terrain correction channels by virtue of positional inaccuracy are not removed from these channels and will be present in any data corrected with them. Further, filtering applied in creating the uncorrected, transformed data is not applied to the terrain correction channels. Mixing data filtered in different ways is not advised.

An alternative method (valid only for datasets where waterbody(ies) have not been taken into account when computing the terrain corrections) uses the linear relationship between the terrain corrections at different densities and the corresponding gravity gradient or $\mathbf{g_D}$ values. This method can be applied to either the grid data or the located data. An example is given using $\mathbf{G_{DD}}$:

The new density is referred to as ρ_N, the existing densities as ρ_1 and ρ_2

$$G_{DD}(\rho_N) = G_{DD}(\rho_1) + \left(G_{DD}(\rho_2) - G_{DD}(\rho_1)\right) \times \frac{(\rho_N - \rho_1)}{(\rho_2 - \rho_1)}$$

Note that the terrain correction channel is eliminated by substitution in deriving this equation.

It is recommended that two densities that differ by a reasonable value be used for this method, in order to minimise uncertainties caused by noise in the data. The values of 0.00 and 2.67 g/cm^3 usually delivered should be sufficient to yield useful results.

When the effect of waterbodies are included in deriving the terrain corrections (bathymetry data have been supplied, enabling the creation of a combined bathymetry and elevation grid to be used for the terrain correction); an alternative

method is required. This method requires waterbody corrected gradients, or $\mathbf{g_D}$, as part of the equation, rather than the ρ_1 data.

The new density is referred to as ρN, the existing density is $\rho 2$ and *WB* refers to the supplied waterbody corrected data.

$$G_{DD}(\rho_N) = G_{DD_{WB}} + \left(G_{DD}(\rho_2) - G_{DD_{WB}}\right) \times \frac{(\rho_N)}{(\rho_2)}$$

8.13 Noise & Signal

By taking two independent measurements of the NE and UV curvature components at each sample point, it is possible to obtain a direct indication of the reliability of these measurements. The standard deviation of half the difference of the pairs of measurements - (A_{NE},B_{NE}) and (A_{UV},B_{UV}) - provides a good estimate of the survey noise:

$$Noise_{NE} = StdDev\left(\frac{(A_{NE} - B_{NE})}{2}\right)$$

$$Noise_{UV} = StdDev\left(\frac{(A_{UV} - B_{UV})}{2}\right)$$

These difference channels are calculated for each data point. The standard deviation across all data points is the figure quoted for the survey as a whole.

This difference error has been demonstrated to follow a 'normal' or Gaussian statistical distribution, with a mean of zero. Therefore, the bulk of the population (95%) will lie between -2σ and +2σ of the mean. For a typical survey noise estimate of, say, 3 E, 95% of the noise will be between -6 E and +6 E.

These typical errors in the curvature gradients translate to errors in $\mathbf{G_{DD}}$ of about 5 E and in $\mathbf{g_D}$ (in the shorter wavelengths) in the order of 0.1 mGal.

8.14 Risk Criteria in Interpretation

The risks associated with a **HeliFALCON™** AGG survey are mainly controlled by the following factors.

- **Survey edge anomalies** – the transformation from measured curvature gradients to vertical gradient and vertical gravity gradient is subject to edge effects. Hence, any anomalies located within about 2 x line spacing of the edge of the survey boundaries should be treated with caution.
- **Single line anomalies** – for a wide-spaced survey, an anomaly may be present on only one line. Although it might be a genuine anomaly, the interpreter should note that no two-dimensional control can be applied.
- **Low amplitude (less than 2σ) anomalies** – Are within the noise envelope and need to be treated with caution if they are single line anomalies and close in diameter to the cut-off wavelengths used.
- **Residual topographic error anomalies** – Inaccurate topographic correction either due to inaccurate DTM or local terrain density variations may produce anomalies. Comparing the DTM with the G_{DD} map terrain-corrected for different densities is a reliable way to confirm the legitimacy of an anomaly.
- **The low density of water and lake sediments** – (if present) can create significant gravity and gravity gradient lows, which may be unrelated to bedrock geology. It is recommended that all anomalies located within lakes or under water be treated with caution and assessed with bathymetry if available.

8.15 References

Boggs, D. B. and Dransfield, M. H., 2004, Analysis of errors in gravity derived from the Falcon® airborne gravity gradiometer, Lane, R. (ed.), Airborne Gravity 2004 - Abstracts from the ASEG-PESA Airborne Gravity 2004 Workshop, Geoscience Australia Record 2004/18, 135-141.

Christensen A.N., Dransfield, M. H. and Van Galder C, 2015, Noise and repeatability of airborne gravity gradiometry, First Break, Volume 33, April 2015, 55 - 63.

Dransfield, M. H., 2010, Conforming Falcon gravity and the global gravity anomaly, Geophysical Prospecting, 58, 469-483.

Dransfield, M. H. and Lee, J. B., 2004, The Falcon® airborne gravity gradiometer survey systems, Lane, R. (ed.), Airborne Gravity 2004 - Abstracts from the ASEG-PESA Airborne Gravity 2004 Workshop, Geoscience Australia Record 2004/18, 15-19.

Dransfield, M. H. and Zeng, Y., Airborne gravity gradiometry: terrain corrections and elevation error, Geophysics 2009/Sep 74(5).

Lee, J. B., 2001, FALCON Gravity Gradiometer Technology, Exploration Geophysics, 32, 75-79.

Lee, J. B.; Liu, G.; Rose, M.; Dransfield, M.; Mahanta, A.; Christensen, A. and Stone, P., 2001, High resolution gravity surveys from a fixed wing aircraft, Geoscience and Remote Sensing Symposium, 2001. IGARSS '01. IEEE 2001 International, 3, 1327-1331.

Stone, P. M. and Simsky, A., 2001, Constructing high resolution DEMs from Airborne Laser Scanner Data, Preview, Extended Abstracts: ASEG 15th Geophysical Conference and Exhibition, August 2001, Brisbane, 93, 99.

9 APPENDIX IV - FINAL PRODUCTS

Final **HeliFALCON™** AGG digital line data were provided in Geosoft Oasis GDB database files containing the fields and format described in *Table 4* below.

Final aeromagnetic digital line data were provided in Geosoft Oasis GDB database files containing the fields and format described in *Table 5* below.

Grids of AGG products, final magnetic intensity, first vertical derivative of the final magnetic intensity, as well as the DTM were delivered, as described in *Table 6* below. The grids are in ERMapper ERS formats with a 25 m cell size, with the exception of the DTM grids which have a 10 m cell size.

One copy of the digital archives was delivered along with a copy of this Logistics and Processing Report.

Channel Name	Description	Units
ALTITUDE	Aircraft DGPS height above EGM96 Geoid	metres
ALTITUDE_DTM	Sensor altitude above DTM ground surface	metres
ALTITUDE_ELLIPSOID	Aircraft DGPS height above WGS-84 Ellipsoid	metres
ANE_0p0	Measured A complement GNE gravity gradient not terrain corrected	eotvos
ANE_2p67	Measured A complement GNE gravity gradient terrain corrected at 2.67 gcc	eotvos
AUV_0p0	Measured A complement GUV gravity gradient not terrain corrected	eotvos
AUV_2p67	Measured A complement GUV gravity gradient terrain corrected at 2.67 gcc	eotvos
BNE_0p0	Measured B complement GNE gravity gradient not terrain corrected	eotvos
BNE_2p67	Measured B complement GNE gravity gradient terrain corrected at 2.67 gcc	eotvos
BUV_0p0	Measured B complement GUV gravity gradient not terrain corrected	eotvos
BUV_2p67	Measured B complement GUV gravity gradient terrain corrected at 2.67 gcc	eotvos
DATE	Flight date	YYYY/MM/DD
DRAPESURFACE	Drape surface for reconstruction	metres
DTM	Terrain Surface Elevation relative to EGM96 Geoid	metres
EASTING	DGPS located X WGS-84 UTM Zone 16N	metres
FLIGHT	Flight number	
gD_0p0	Vertical gravity with no terrain correction applied	mGal
gD_0p0_conformed	Vertical gravity with no terrain correction applied conformed to regional data	mGal
gD_2p2	Vertical gravity corrected using a density of 2.2 gcc	mGal
gD_2p2_conformed	Vertical gravity corrected using a density of 2.2 gcc conformed to regional data	mGal
gD_2p67	Vertical gravity corrected using a density of 2.67 gcc	mGal
gD_2p67_conformed	Vertical gravity corrected using a density of 2.67 gcc conformed to regional data	mGal
GDD_0p0	Vertical gravity gradient with no terrain correction applied	eotvos
GDD_2p2	Vertical gravity gradient corrected using a density of 2.2 gcc	eotvos
GDD_2p67	Vertical gravity gradient corrected using a density of 2.67 gcc	eotvos
GED_0p0	GED gradient with no terrain correction applied	eotvos
GED_2p2	GED gradient corrected using a density of 2.2 gcc	eotvos
GED_2p67	GED gradient corrected using a density of 2.67 gcc	eotvos
GEE_0p0	GEE gradient with no terrain correction applied	eotvos
GEE_2p2	GEE gradient corrected using a density of 2.2 gcc	eotvos
GEE_2p67	GEE gradient corrected using a density of 2.67 gcc	eotvos
GND_0p0	GND gradient with no terrain correction applied	eotvos
GND_2p2	GND gradient corrected using a density of 2.2 gcc	eotvos
GND_2p67	GND gradient corrected using a density of 2.67 gcc	eotvos
GNE_0p0	GNE gradient with no terrain correction applied	eotvos

GNE_2p2	GNE gradient corrected using a density of 2.2 gcc	eotvos
GNE_2p67	GNE gradient corrected using a density of 2.67 gcc	eotvos
GNN_0p0	GNN gradient with no terrain correction applied	eotvos
GNN_2p2	GNN gradient corrected using a density of 2.2 gcc	eotvos
GNN_2p67	GNN gradient corrected using a density of 2.67 gcc	eotvos
GUV_0p0	GUV gradient with no terrain correction applied	eotvos
GUV_2p2	GUV gradient corrected using a density of 2.2 gcc	eotvos
GUV_2p67	GUV gradient corrected using a density of 2.67 gcc	eotvos
LATITUDE	DGPS located Latitude WGS-84	degrees
LINE	Line number	
LONGITUDE	DGPS located Longitude WGS-84	degrees
NORTHING	DGPS located Y WGS-84 UTM Zone 16N	metres
T_DD	Terrain effect calculated for DD (assumes density correction of 1 gcc)	eotvos
T_NE	Terrain effect calculated for NE (assumes density correction of 1 gcc)	eotvos
T_UV	Terrain effect calculated for UV (assumes density correction of 1 gcc)	eotvos
TURBULENCE	Aircraft turbulence	milli-g
UTC_TIME1980	UTC Time (seconds since 1980)	seconds

Table 4: Final HeliFALCON™ AGG Digital Data –Geosoft Database Format

Channel Name	Description	Units
ALTITUDE	Aircraft DGPS height above EGM96 Geoid	metres
ALTITUDE_DTM	Sensor altitude above DTM ground surface	metres
COMPMAG	Lagged, despiked, compensated TMI	nanoteslas
DATE	Flight date	YYYY/MM/DD
DCMAG	COMPMAG after subtraction of the IGRF and DIURNAL	nanoteslas
DIURNAL	De-spiked, lightly filtered base station mag	nanoteslas
DTM	Terrain Surface Elevation relative to EGM96 Geoid	
EASTING	DGPS located X WGS-84 UTM Zone 16N	metres
FLIGHT	Flight number	
FLUX_X	Fluxgate X Component	nanoteslas
FLUX_Y	Fluxgate Y Component	nanoteslas
FLUX_Z	Fluxgate Z Component	nanoteslas
IGRF	IGRF based on date and position of each point	nanoteslas
LATITUDE	DGPS located Latitude WGS-84	degrees
LEVMAG	Leveled and micro-leveled DCMAG	nanoteslas
LEVMAG_1VD	First Vertical Derivative of leveled and micro-leveled DCMAG	nanoteslas/metre
LINE	Line number	
LONGITUDE	DGPS located Longitude WGS-84	degrees
NORTHING	DGPS located Y WGS-84 UTM Zone 16N	metres
RAWMAG	Lagged uncompensated unfiltered TMI	nanoteslas
UTC_TIME1980	UTC Time (seconds since 1980)	seconds

Table 5: Final Aeromagnetic Digital Data –Geosoft Database Format

Grid Name	Description	Units
2200072_DTM	Terrain Surface Elevation relative to EGM96 Geoid	metres
2200072_gD_0p0_final	Vertical gravity with no terrain correction applied	mGal
2200072_gD_0p0_conformed_final	Vertical gravity with no terrain correction applied conformed to regional data	mGal
2200072_gD_2p2_final	Vertical gravity corrected using a density of 2.2 gcc	mGal
2200072_gD_2p2_conformed_final	Vertical gravity corrected using a density of 2.2 gcc conformed to regional data	mGal
2200072_gD_2p67_final	Vertical gravity corrected using a density of 2.67 gcc	mGal
2200072_gD_2p67_conformed_final	Vertical gravity corrected using a density of 2.67 gcc conformed to regional data	mGal
2200072_GDD_0p0_final	Vertical gravity gradient with no terrain correction applied	eotvos
2200072_GDD_2p2_final	Vertical gravity gradient corrected using a density of 2.2 gcc	eotvos
2200072_GDD_2p67_final	Vertical gravity gradient corrected using a density of 2.67 gcc	eotvos
2200072_LEVMAG_final	Leveled and micro-leveled DCMAG	nanoteslas
2200072_LEVMAG_1VD_final	First Vertical Derivative of leveled and micro-leveled DCMAG	nanoteslas/metre

Table 6: Final Aeromagnetic and FALCON® AGG Grids –ERMapper Format

APPENDIX B: Flight Line Map

Crystal Lake Project HeliFalcon Flight Lines and Land Tenure

Legend

- HeliFalcon Flight Lines
- Highway
- Secondary Road

Land Tenure Type

- Mining Claim
- Patent
- Lease

Pardee Twp.

Devon Twp.

Crooks Twp.

Oliver Lake

Crystal Lake

Lake Lenore

Lake Superior

U.S.A

HWY 61

503170 503171 503172 503173 503174 503175
503176 503177 503178 503179 503180 503181
503182 503183 503184
503185 503186 503187

PAT-17418

PAT-17417
280459 299132 280458

PAT-17422
PAT-17421
299133 327716 327715
PAT-17420
224503 159615 119253

PAT-17423
LEA-108295
LEA-108293
LEA-108298
LEA-108872
LEA-108296
LEA-109044
LEA-109045
LEA-109049
LEA-108297
LEA-108300
LEA-108873
LEA-109047
LEA-109048

239765 139024 110051 335223 191640 139023
335224 145021 211120 307079 307078 211119
124539 291891 343456 260509 308690 128615 308689 192101
235869 181979 136010 248840 104972 229329 242016 323833
124541 124540 152427
304579 181980 124542

PAT-17429
PAT-17431
PAT-17430
PAT-17432
PAT-17433
PAT-17427
PAT-17428
PAT-50924

LEA-108301
LEA-108871
LEA-108294
LEA-108870
LEA-108869
LEA-108868
LEA-108866
LEA-108874
LEA-109983
LEA-110023

PAT-17426
PAT-17425
PAT-17424
PAT-16406
PAT-50925

232744 161399 215577 131292
269465 104609 223095 104608 104607 177209 167767
156493 279077 163807 279076 279075 243263 290608 205837 172290 228474 275699
208449 243264 157720 338725 278308 253674 108756 245608 209056 220485 324277
122207 338726 326337 118559 122961 319662 178919 127694 174536 324278
192161 314869 335735 198516 253675 319663 282850 172291 209057 190566
335736 107491 128099 274461
125472 305445 142961 181619
292774 218833 142962
125473 312196 137462

639535
263678 132227
251665 213752

PAT-29083
PAT-29082
PAT-29084
199792 310307
126646 138105 309103 310308 254413
190636 138106 268588 294564 249845
267876 173319 306672 227913 126647 171173
269736 340181 128672 138126 143621
260422 245228 162626 190118 344349 254480 322672
159685 225063 308743 187788 320499 273298 266544
128673 320486 338732 135111 333731 207313
187789 303151 303150

264022 318564 197004 263663
315868 250033 271478 234744 333210
165465 309136 114018 205482 331454
315869 268712 194742 252260 263765 318300
224839 140641 146595 213289 252261 263766 109190
204745 328636 328635 332141 165466 280745 299368 214353
270744 167469 300577 330684
109074

0 2,500 5,000 m

1:35,000
UTM NAD 83 Zone 16U